

INVESTIGATION OF FLUID FLOW BEHAVIOR IN THE HUMAN UPPER AIRWAY DURING INHALATION

Joel Joseph Raco

Master of Research



School of Engineering
Macquarie University

May 23, 2018

Shaokoon Cheng

Contents

Table Of Contents	ii
List Of Figures	iv
List Of Tables	vii
Abstract	viii
Statement Of Originality	ix
Acknowledgements	x
1 Introduction	1
1.1 The Upper Airway Anatomy	2
1.1.1 Oropharynx	2
1.1.2 Laryngopharynx	4
1.1.3 Nasopharynx	5
1.2 Respiratory Flow Physiology	5
1.3 Upper Airway Movement	7
1.4 Reconstruction of 3D Human Upper Airway	8
1.5 Particle Imaging Velocimetry	9
1.6 Summary	10
2 Methods	11
2.1 Phantom Manufacture	11
2.1.1 3D Reconstruction from Image Data	11
2.1.2 Mould Design	15

2.1.3	Mould Manufacture	21
2.1.4	Model Casting	23
2.2	Experimental Setup	27
2.2.1	Flow Circuit	27
2.2.2	Piston Pump	27
2.2.3	Flow Rate	31
2.2.4	Phantom Deformation	33
2.2.5	Electronics Control	34
2.2.6	Tank	34
2.2.7	Phantom	35
2.3	PIV Setup	36
2.4	Computational Fluid Dynamics	37
3	Results	39
3.1	Particle Imaging Velocimetry	39
3.2	Computation Fluid Dynamics	41
4	Discussion And Future Work	44
4.1	Discussion	44
4.2	Future Work	46

Appendices

A	Arduino Electronics Control Code	A-1
----------	---	------------

List of Figures

1.1	Upper airway anatomy [1].	2
1.2	Movement of the epiglottis during respiration [2].	4
1.3	A comparison of inspiration time and expiration time. As seen, the cycle follows a sinusoidal form with an extended expiration period [3].	6
1.4	Lung capacities.	6
1.5	How the motion of the epiglottis is affected by a persons BMI [4].	8
1.6	PIV setup example [5].	10
2.1	3D Slicer User Interface. The current module, segment editor, is shown near the top left of the page, adjacent to the save and load options. On the right near the top is the extension manager which can provide additional segmentation tools. On the left, the effects that can be used in the segmentation process are shown, in addition to a toggle to show the 3D result of that segmentation. Finally, the lower right region shows the volume currently being used for segmentation in the orthogonal views and a 3D rendering of the segmentation. In this region, the selected voxels are colored and represent the region of interest as constructed using the module effects.	14
2.2	Prepared inner lumen with cylindrical inlet and outlet, in addition to alignment dovetails. The shell looks identical however, the cylinders are larger by the wall thickness of the phantom and it does not yet possess alignment dovetails. The inner lumen is one part of the three-part mould used to cast the silicone phantom.	16
2.3	The pull direction is indicated by the arrows connected to each mould half. Each mould half can pull away from the other as there are no physical obstructions to prevent this from occurring.	17

2.4	A simulation of undercut formation in a single plane of an arbitrary mould as it is filled with a fluid.	18
2.5	All mould pieces after completing the design process. Note that this design has been updated and does not reflect the cast phantoms used for the results as they were cast using a previous mould design.	20
2.6	Process of smoothing the rapid-prototyped parts using a vapor chamber filled with solvent and temperature maintained at the parts distortion temperature.	23
2.7	The inner lumen is placed inside each mould half prior to casting to verify its position with respects to the mould halves. As can be seen, the inner lumen does not touch the mould halves at any point along its length.	24
2.8	The process of mixing and degassing the silicone rubber prior to casting.	25
2.9	Mould before and after casting.	26
2.10	The piston pump provides oscillatory flow controlled by a stepper motor. The ball valve connected to the pump allows the pump to be isolated and drained when not in use. In addition, the second line containing a ball valve is used to drain the tank after use. The phantom is submerged in a tank and connected to the pump and reservoir, the fluid inside these areas contains tracer particles.	27
2.11	CAD drawings of the linear actuator components.	28
2.12	Linear actuator assembly in CAD.	29
2.13	Piston components.	29
2.14	Piston pump assembly in CAD.	30
2.15	Piston pump setup, note that a reducer is added to the end of the bore in order to facilitate a 25 mm polytube for fixing to the remainder of the setup. All connections are either cemented using PVC cement or threaded with British Standard Pipe (BSP) fittings and Teflon tape. The polytube is fitted with a hose clamp.	30
2.16	Actuator rail system to suit two Actuonix L12 actuators for use in deforming the phantom.	33
2.17	Tank and t-slot stand with flow circuit connections on the bottom panel and sealed plugs on the side panels.	35

2.18	Phantom in the tank with water-glycerol mixture. PIV equipment setup with laser sheet in the sagittal plane and camera pointing perpendicularly to the sheet.	37
3.1	Velocity vector profile in the sagittal plane with constant inspiratory flow rate. The vector size indicates the magnitude of the velocity. The uvula and epiglottis can be seen at the top right and bottom right of the figure respectively. The outline was created through the use of a mask and is an indication of the phantom wall.	40
3.2	Velocity vector profile in sagittal plane with a flow rate of $30 \frac{L}{min}$ of air. . . .	41
3.3	Velocity contours in the axial plane from CFD simulations with a flow rate of $30 \frac{L}{min}$ of air at various points along the length of the pharynx.	42
3.4	Velocity and Pressure contours in the sagittal plane from CFD simulations with a flow rate of $30 \frac{L}{min}$ of air.	43

List of Tables

2.1	Breakdown of the costs and time required to rapid prototype the mould used to cast the silicone phantom.	22
-----	---	----

Abstract

Despite the array of studies on respiratory flow modeling, very few experimental works have been conducted to validate the results of the models. The objective of this research sets the groundwork for a comprehensive study on upper airway mechanics. Briefly, this thesis documents the work which has been undertaken during this 8-month research program and is summarised as such. A method to reconstruct models of human organs using 3D Slicer, an open source software. A novel method to develop an airway phantom with highly complex geometry. Design and development of a flow circuit capable of simulating a range of flow conditions. Design and development of an organ grip to simulate moving wall boundary conditions. Design and development of a particle image velocimetry (PIV) tank and other accessories. Finally, the development of a computational model to determine and match the experimental flow field obtained using PIV. This research presents analogous results of the flow field determined from the PIV experiment and computational model in specific locations of the upper airway. Further studies to determine the effect of physiologically realistic complex airway deformation and flow using the developed tools are necessary to help improve our current knowledge in respiratory mechanics and flow.

Statement Of Originality

This work has not previously been submitted for a degree or diploma in any university. To the best of my knowledge and belief, the thesis contains no material previously published or written by another person except where due reference is made in the thesis itself.

Joel Joseph Raco

Candidate's Name

Signature

/ /

Date

Acknowledgements

I would like to thank and acknowledge all my mentors and colleagues who have helped and encouraged me during the past 8 months while undertaking this research.

Firstly, I would like to thank my supervisor, Shaokoon Cheng for his guidance and advice.

Secondly, I would like to thank my colleges Sajjad Mahmoudi, Taye Mekonnen and Lingmeng Li for their support during this time.

Chapter 1

Introduction

Respiration is key to survival, and hence the human respiratory tract is the conduit of life. Respiratory physiology in humans encompasses a series of highly complex events including the exchange of air and movement of oxygen from the outside environment to the cells within tissues. This oxygen is necessary for cells to transfer energy stored in food to a usable form, hence, enabling their respective organs to function. For example, the heart will stop functioning when the muscles are deprived of oxygen, leading to cell and organism death. Therefore, adequate air flow into the lungs is essential and the disruption of this process is known to play critical roles in the development or aggravation of diseases such as chronic obstructive pulmonary disease, asthma, and obstructive sleep apnea [6]. Not surprisingly, the aforementioned diseases, as some of their names imply, are related to the obstruction of airflow along the respiratory tracts, and while the general mechanisms of the diseases are known [7–9], lack of detailed information on how alteration of flow mechanics contribute to some of the disease mechanisms remains completely unclear. For example, obstructive sleep apnea is a disease that is characterized by the repetitive collapse of the human upper airway during sleep, and although collapsation of the upper airway has been widely known to be caused by reduced airway muscular activity during sleep, how change in airflow mechanics alter the pressure in the airway to promote the collapsation is unclear and has been a growing area of research interest in recent years [10].

This research project forms part of a Ph.D. program where the goal is to understanding air flow mechanics in the human upper airway through the use of particle image velocimetry (PIV). While computational models have been largely used to simulate air flow in the respiratory tracts, many of the models which produced interesting images of flow fields have not

been validated against experimental data. More importantly, due to the existing inherent limitations of the computational models, all of the models have assumed rigid airway walls even though several imaging studies have convincingly demonstrated that the geometry of the human upper airway deforms dynamically during respiration and especially during deep inhalation [4, 11, 12]. Such dynamic airway wall movement will potentially influence the flow field and is likely to shed light on airflow mechanics which may have implications in understanding drug delivery or airway collapse mechanisms. Hence, an experimental design to undertake this research is necessary and this project has produced several critical outputs that form the foundation for the research to be undertaken.

1.1 The Upper Airway Anatomy

The upper airway consists of the pharynx, the nasal cavities, and whether it includes the larynx and trachea in this general definition remains controversial. Nevertheless, the term pharynx which is also known as the throat can be perceived as a conduit that comprises 3 main sections, namely, the oropharynx, nasopharynx, and laryngopharynx, see figure 1.1.

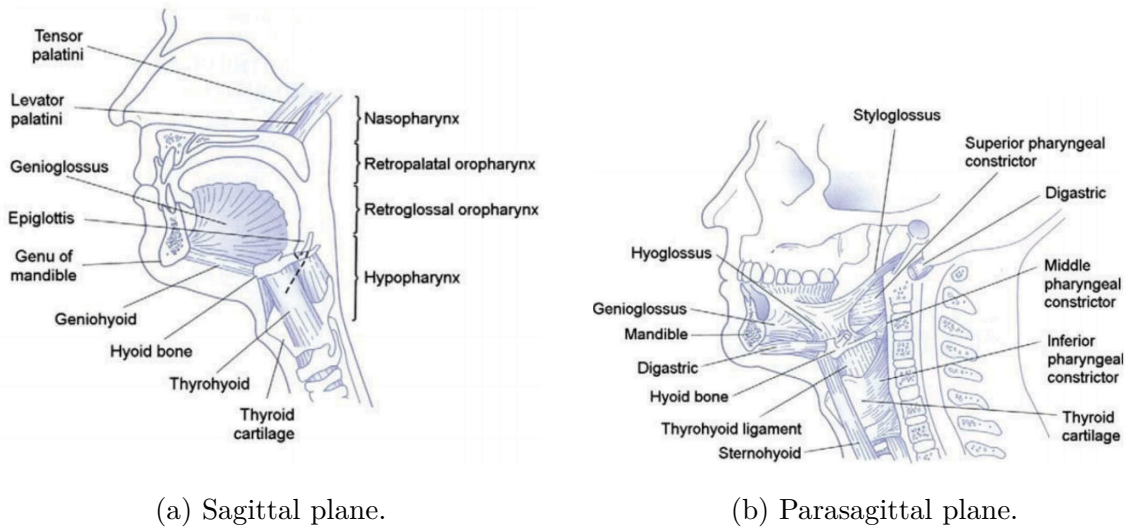


Figure 1.1: Upper airway anatomy [1].

1.1.1 Oropharynx

The oropharynx is basically the part of the pharynx that is between the soft palate and hyoid bone. In humans, the posterior oropharynx is the part of the airway that can be seen

directly when the mouth is opened. An important thing to note is that the structure of the oropharynx is basically defined by the surrounding soft tissues with the tongue as the major organ that forms the anterior part of this complex geometry. Hence, the geometry of oropharynx changes dynamically and is distinctively different during swallowing, speech and breathing as the tongue muscle deforms and changes shape to perform these complex tasks. Such complex deformation of the tongue is made possible by the fact that the organ is made of 8 different sets of muscles with very different muscle fiber orientations and nervous innervations which determines their activities from neuromuscular drive [13,14]. Collectively, a variety of intricate but well-controlled movements such as retraction, protrusion, elevation and depression alter both the shape and stiffness of the tongue and are made possible by these muscles [15]. Indeed, as the tongue is unattached on one end, it can move with an unlimited degrees of freedom which further demonstrates that the geometry of the oropharynx is highly deformable [16]. However, it is important to note that the tongue is incompressible and hence, it behaves as a muscular hydrostat and the overall volume of the organ is conserved at different states. This implies that despite the plausible complex changes in oropharynx geometry [17], the upper airway volume is unlikely to change significantly. For example, research shows that the lateral collapse of the human upper airway at the cranial part of the oropharynx is usually accompanied by the anterior-posterior lengthening of the airway dimensions [4, 11, 12].

In addition to the tongue, the uvula is another distinctive structure of the oropharynx. The uvular is basically a fleshy, cone-like shape tissue that is attached to the soft palate back portion. The primary function of the uvular is that it acts as a valve and moves with the soft palate to close off the nasopharynx during swallowing to prevent food from entering into the nasal cavity [18]. The uvular is also largely responsible for the secretion of large amounts of saliva to help moisturise the throat [19], which is also critical in trapping foreign particles and allowing food to be swallowed. Other functions of the uvula include its role in triggering gag reflexes (contraction at the back of the throat to prevent choking) and as an induction site for mucosal intolerance from inhaled antigens [20]. As the surrounding soft tissues of the oropharynx, including the tongue, consists of fats, the intrinsic dimensions of the oropharynx, such as airway diameter, could decrease with increase in body mass index (BMI) and this results in narrower air space between the uvula and the back pharyngeal wall. Indeed, even though the uvular presents several important and useful functions in upper airway physiology,

they have also been known to cause obstructive sleep apnea [21]. Uvulopalatopharyngoplasty is the surgical procedure to remove the uvula tissues as a treatment modality for obstructive sleep apnea but the effectiveness of this treatment remains controversial [22].

1.1.2 Laryngopharynx

The laryngopharynx is the lower part of the pharynx and connects the pharynx with the esophagus and extends from the upper tip of the epiglottis. The role of the laryngopharynx is significant and works as a conduit that separates food and air and this is largely performed by the epiglottis. The epiglottis is a leaf-shaped flap of elastic cartilage located behind the tongue and helps to seal the trachea during eating to prevent food from getting into the lung. The location of the epiglottis is hence controlled by the tongue muscle. Although the epiglottis is known to stand open in a pseudo vertical position during breathing, recent studies have repeatedly demonstrated that it moves anteriorly to open the airway during inspiration [12]. During swallowing, the hyoid bone is elevated and this draws the larynx slightly upwards and causes the epiglottis to collapse to a horizontal position to cover the windpipe such that the superior side of the structure forms part of the upper airway, see figure 1.2 [2]. As mentioned, the tongue plays an obvious role in such a complex maneuver.

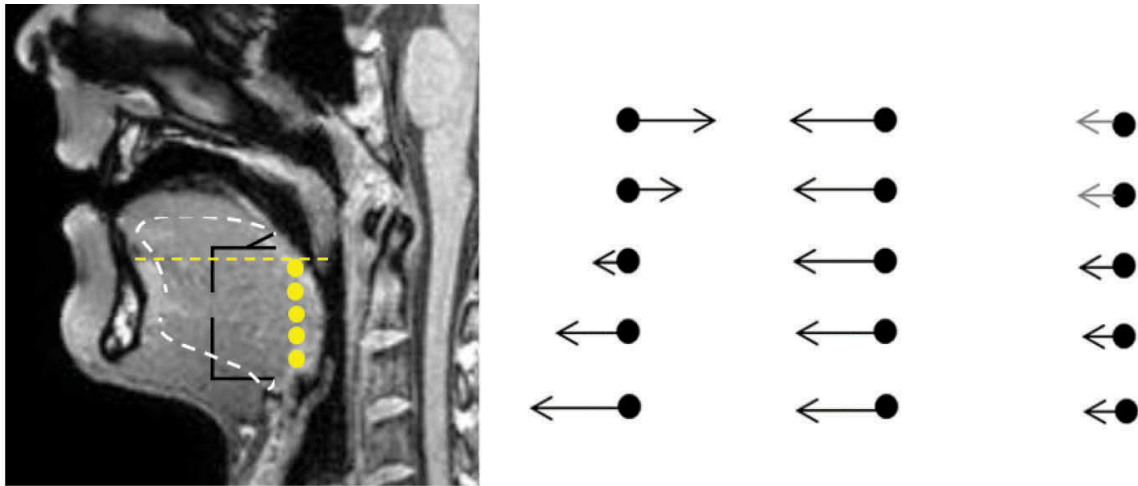


Figure 1.2: Movement of the epiglottis during respiration [2].

1.1.3 Nasopharynx

The nasopharynx is the upper part of the pharynx that connects with the nasal cavity above the soft palate. Located behind the nasal fossa and within the occipital bone, this part of the pharynx is less deformable compared to the oropharynx and laryngopharynx and is typically confined within a volume of 17.5 cm^3 in a typical human [23].

1.2 Respiratory Flow Physiology

Air enters the lungs via the nose or mouth, the mechanics are complex and involve the activation of several respiratory muscles and the elastic recoil of these soft tissues. For example, to inflate the lungs during inhalation in humans, an increase in the volume of the thoracic cavity is required and this is made possible by the contraction of the diaphragm muscle and the intercostal muscles which helps elevate the rib cage. During exhalation, the muscle relaxes and this helps the muscles to return to their original position and this is largely determined by the tissue elasticity and also the patency of the respiratory tracts [24]. Hence, whilst inspiration is an active process, expiration is passive and the ratio of duration between inspiration and expiration is 1:2 or lesser during tidal breathing [3]. Air flow velocity profile in humans is hence cyclical in nature and can be represented by a Fourier series, see figure 1.3. The average human respiratory rate is between 12 to 20 breaths per minute in adults and lung volume and lung capacities, which can be measured using a spirometer, are typically illustrated in the chart as shown in figure 1.4. The figure shows the volume of air exchange during different breathing maneuvers. For example, tidal volume is the volume of air that is inhaled or exhaled in a single breath. Therefore, an average adult inhales 7 to 8 liters of air per minute [3].

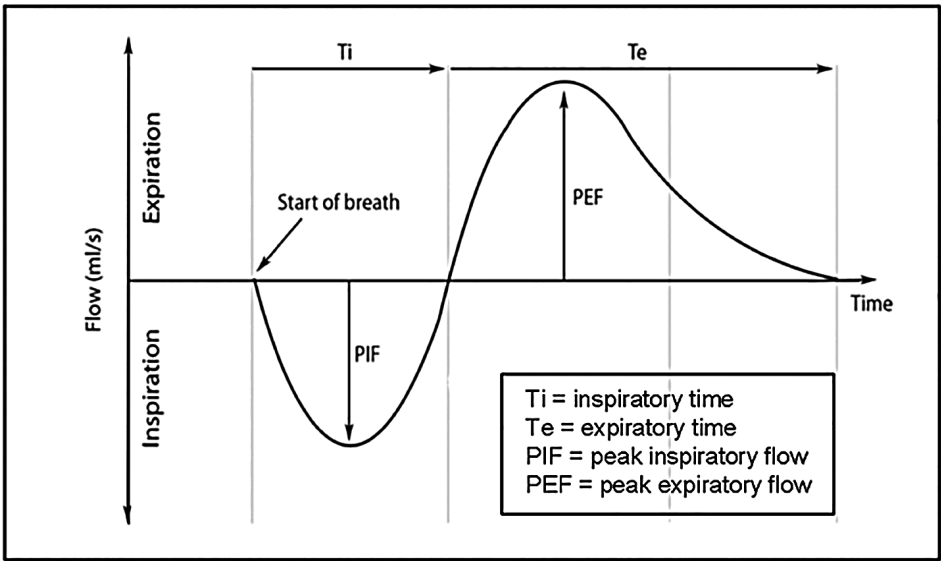


Figure 1.3: A comparison of inspiration time and expiration time. As seen, the cycle follows a sinusoidal form with an extended expiration period [3].

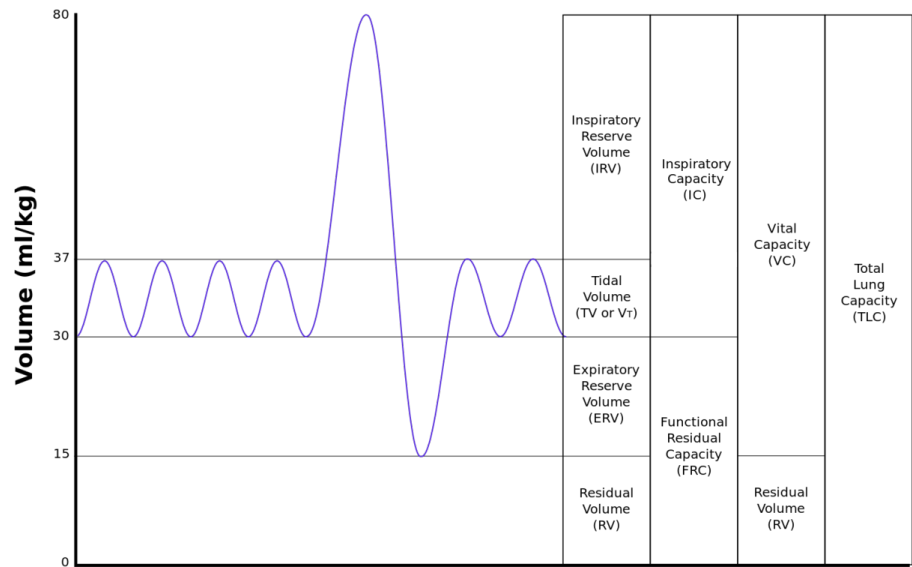


Figure 1.4: Lung capacities.

1.3 Upper Airway Movement

As mentioned earlier, while the oropharynx is highly deformable, the nose, larynx, and trachea are more rigid as they are formed by frameworks of cartilage [25]. In this section, a detailed review of how the upper airway deforms during breathing will be presented. Figure 1.1 shows a picture of the various muscle sets that form the tongue. As one can easily observe, the genioglossus is the major muscle of the tongue and is known as the primary protruding muscle. Numerous research endeavors have been carried out in an effort to understand the genioglossus due to its obvious role in obstructive sleep apnea [26, 27]. As the tongue does not have a skeleton, the genioglossus, like other tongue muscles, are activated and controlled by neuromuscular activity, similar to the trunk of elephants. Hence, not surprisingly, the activity in the genioglossus has been demonstrated to be significantly lower during sleep [28]. The significant reduction in the muscle activity and the weight of the tongue during sleep underpins the primary mechanics for airflow obstruction in obstructive sleep apnea [29]. Muscle activity in the genioglossus is measured via electromyography (EMG) and although this method is an invasive procedure, it has shed light on how the upper airway maintains patency during breathing due to its high temporal resolution [30–32]. However, the greatest setback with this primitive technique is that it is unable to provide information on tissue motion since the increase in EMG activity in the tongue could imply that the tissue has increased in stiffness or deformed.

The visual demonstration of how the upper airway deforms during breathing has only been made possible by using advanced magnetic resonance imaging (MRI) [11]. Cheng shows that during inspiration, the genioglossus moves forward to open the airway at the level of the epiglottis to enable air flow. Such tissue motion varies between individuals and is dependent on the intrinsic size of the upper airway and other craniofacial feature dimensions [33]. A typical chart which shows how the motion increases non-linearly with airway size is shown in figure 1.5. Another study by Cheng also shows that deformation of the upper airway boundaries is not consistent between individuals and is underpinned by a number of patterns which have been further demonstrated to be similar in patients with sleep apnea [4]. There is a complete lack of information on how these different patterns of moving boundaries affect air flow dynamics and therefore, the aim of this research is to understand and fill the knowledge gap in this area through the use of optically accessible

silicone phantoms and PIV.

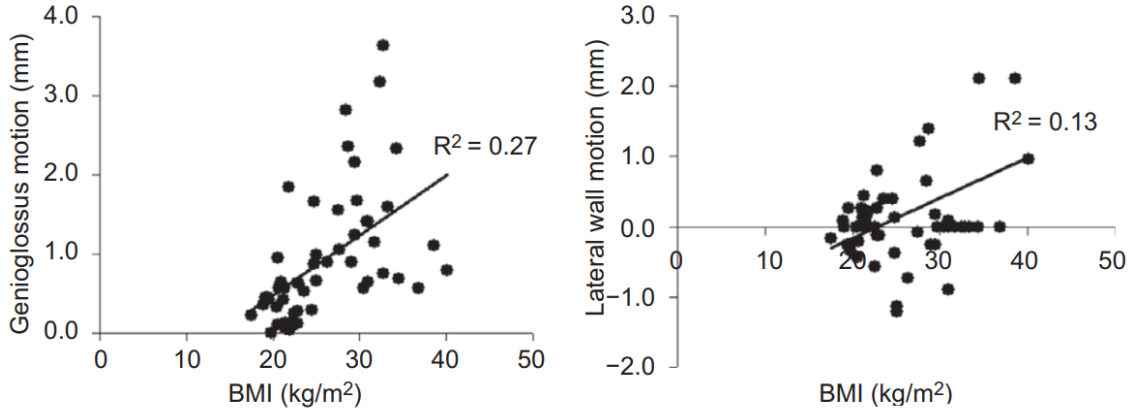


Figure 1.5: How the motion of the epiglottis is affected by a persons BMI [4].

1.4 Reconstruction of 3D Human Upper Airway

The process to create physical 3D reconstructed models of a human's organs have been made easier with the introduction of commercialized software packages. However, many of the software packages are expensive and require post-processing. Typically, the user is required to mark or segment the region of interest using a set of 3D images acquired using MRI or CT technologies. While some of the costlier software enables segmentation to be performed automatically, semi-automatically and manually, others are limited in this function. It is important to understand that a semi-automatic approach is often useful in 3D reconstruction given that the boundaries of the anatomy can be blurry or not well defined due to artifacts from movement during imaging. Traditionally, a segmented organ is presented as an image stack when exported to a typical computer aided program and surfacing skills are required to build a model. This can become highly time consuming when the organ of interest is non-symmetrical and organic in shape. This has been largely resolved in commercialized software packages, however, in this research project, a low cost open source approach to reconstruct 3D models of the human upper airway is proposed which will form part of the methodology to manufacture airway phantoms.

The methods for manufacturing a structure with a highly complex geometry are not very well documented in the literature. While casting has been generally known as the primary method to manufacture the replicas [34], the primary complication lies in the fact that there

are severe undercuts in some organs which makes it very difficult to define the parting line for the mould. This is further complicated if the organ of interest is a conduit as the mould will require additional components, which will need to be registered and dissolved as part of the moulding and demoulding process respectively. In essence, the manufacturing of a complex organ phantom like the upper airway is time-consuming and requires trial and error as it is an interplay between the tolerance of the cast, material of the cast and the percentage constituents of the silicone material which affects its rheological properties. Another goal of this research proposal is to determine the procedure and process in creating an optically accessible upper airway cast suitable to be used in PIV.

1.5 Particle Imaging Velocimetry

PIV is a common method that is used to visualize flow, a typical schematic is presented in figure 1.6. By seeding the fluid with tracer particles that follow the flow dynamics, this method enables instantaneous measurements of velocity and flow field. To provide high-quality qualitative and quantitative data, the particles that are entrained in the fluid need to be visible and this is achieved through the use of laser sheets. While other methods such as laser Doppler velocimetry and hot wire anemometry are also able to measure flow [35], these methods only enable point measurements and hence are inferior to PIV in terms of spatial resolution and capabilities. In order to obtain a high quality flow field in the upper airway, it is important to ensure that the silicone that is used to manufacture the upper airway is tuned to ascertain that it is highly optically accessible. Nevertheless, it is also common to ascertain this by using glycerol and water solution as the media to reduce the effects of light refraction when the replica is in a tank filled with fluid [36].

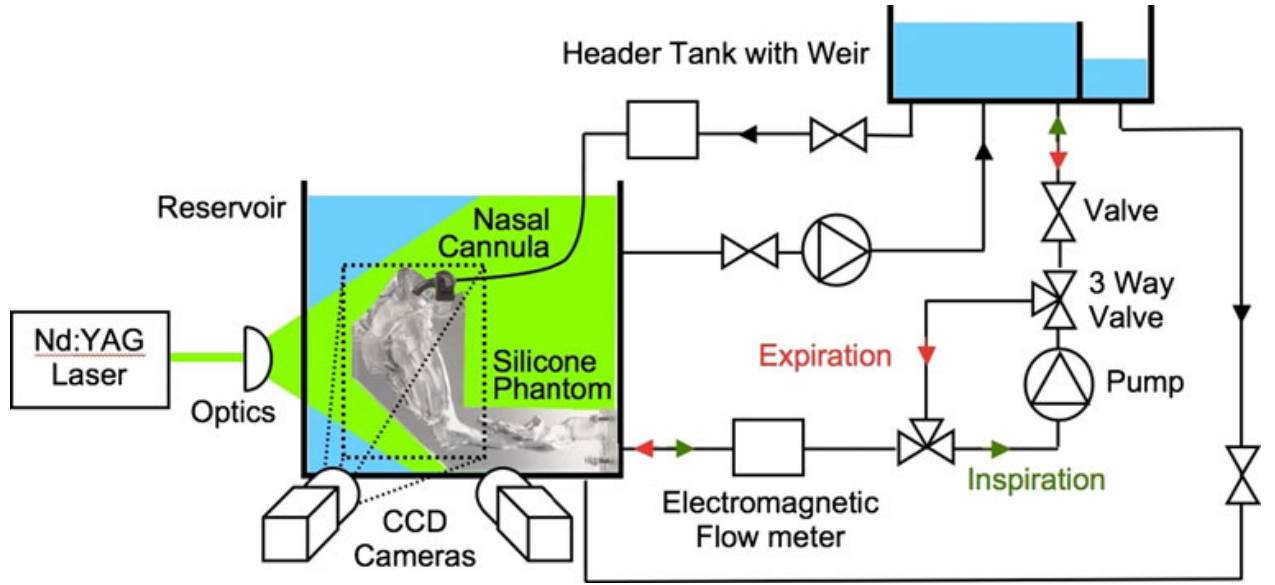


Figure 1.6: PIV setup example [5].

1.6 Summary

In conclusion, very few studies have performed experimental studies of flow in the upper airway and all existing work in this area has neglected the active contraction of the extrathoracic muscles. While there is a plethora of work performed in the computational modeling of upper airway, the realistic physiological deformation of the airway wall was not simulated and fluid structure flow interaction involves a passive airway that more closely represents the state of upper airway during sleep. The above suggests that information on the realistic air flow profile during active inhalation in human remains unclear and this forms the motivation of this study.

Chapter 2

Methods

This chapter will describe the methods involved with the design and manufacture of the PIV system. This will include, the phantom, experimental setup, PIV setup and numerical simulations. It will resolve a variety of problems, which will be discussed later, related to the above by presenting the most suitable solution.

In order to successfully test the whole system an upper airway phantom will be used to collect initial results and these will be compared to the numerical simulation results.

2.1 Phantom Manufacture

2.1.1 3D Reconstruction from Image Data

Open source software, 3D Slicer (<https://www.slicer.org/>) provides sample data (<https://www.slicer.org/wiki/SampleData>) through the National Alliance for Medical Imaging Computing (https://na-mic.org/wiki/Main_Page). An MRI of the head is downloaded from the sample data within 3D Slicer as it depicts the upper airway geometry. 3D Slicer allows the user to view the image data and reconstruct the region of interest; in this case the upper airway. The images are viewed and examined to determine if they contain sufficient detail for use in reconstruction. The primary anatomical features such as the epiglottis and uvula are identified and their level of detail, such as the structure boundary, is examined visually.

3D Slicer accepts a variety of data formats such as DICOM and BMP. All these data types represent a stack of images, with each image having the same dimensions, for example, length and width. The height of the stack is determined by the number of images within

it and the spacing between those images. In addition to the image dimensions, the image stack also has a resolution which corresponds to the size of each voxel (3D pixel). This is important as a collection of selected voxels make up the final 3D model. Hence voxel size is one of the most important factors in the reconstruction process when using 3D Slicer as it determines the smallest detail which can be captured.

All operations carried out in 3D Slicer are done using modules. A selection of modules are made available with 3D Slicer by the developers, however, extensions can be added to increase the functionality of certain modules or create entirely new modules. Extensions can be viewed using the Extensions Manager Wizard and can prove invaluable.

Using 3D Slicer, it is possible to manipulate the stack of images in order to change the voxel size much like scaling the resolution of an image to fit different size monitors. Module, crop volume, is used to alter the voxel size using the interpolation method of one's choosing, in addition to reducing the image dimensions to focus on the region of interest. When increasing the resolution this way it is important to consider the file size as reducing voxel dimensions by half will increase the number of voxels eightfold. Hence, cropping the image stack is useful for reducing the files size. As a guide, voxel size should be such that they can fit within the region of interest with minimal crossing over the edge of the region.

For the airway phantom reconstruction, a voxel size of 0.25 mm cube is used to form an image stack with dimensions of 276 voxels by 448 voxels by 468 voxels (69 mm by 112 mm by 117 mm). This information can be found in the module, volumes, under the heading volume information. It should be noted that the shape of a voxel is limited to a rectangular prism of any dimension.

The 3D mesh model is reconstructed using the module segmentation editor as seen in figure 2.1. Individual voxels are selected in each image using the available effects to form a collection of voxels which describe the location and shape of the region of interest. In order to efficiently and accurately map out the region of interest, the threshold effect is used to select all voxels in a range based on their intensity from white to black. The selection range is altered until the preview shows that the region of interest is fully contained. Since the airway is represented by black voxels, the selection range starts at zero intensity and ends at a dark grey intensity. This selects all the voxels in the region of interest in addition to other undesired voxels that match the intensity range specified. The scissors and island effects are then used in the orthogonal and perspective views to remove unwanted chunks of voxels,

leaving behind only the region of interest.

After the region of interest has been described, the creation of the model shell is required. A phantom wall thickness that is deemed sufficiently thin to deform with ease, but not so much such that it will be too fragile to handle is required. The current segment is first exported as an STL mesh model for use later. The margin effect is then applied to the same segment and its output is a segment that has a wall thickness from the original of half the margin size. It is important to consider if any scaling of the phantom is necessary for the experimental work being carried out as this margin will also be scaled. Once the margin is completed, the preview is inspected for undercuts and effects such as paint and smoothing are applied to the model to remedy them. Finally, this segment is also exported as an STL mesh model.

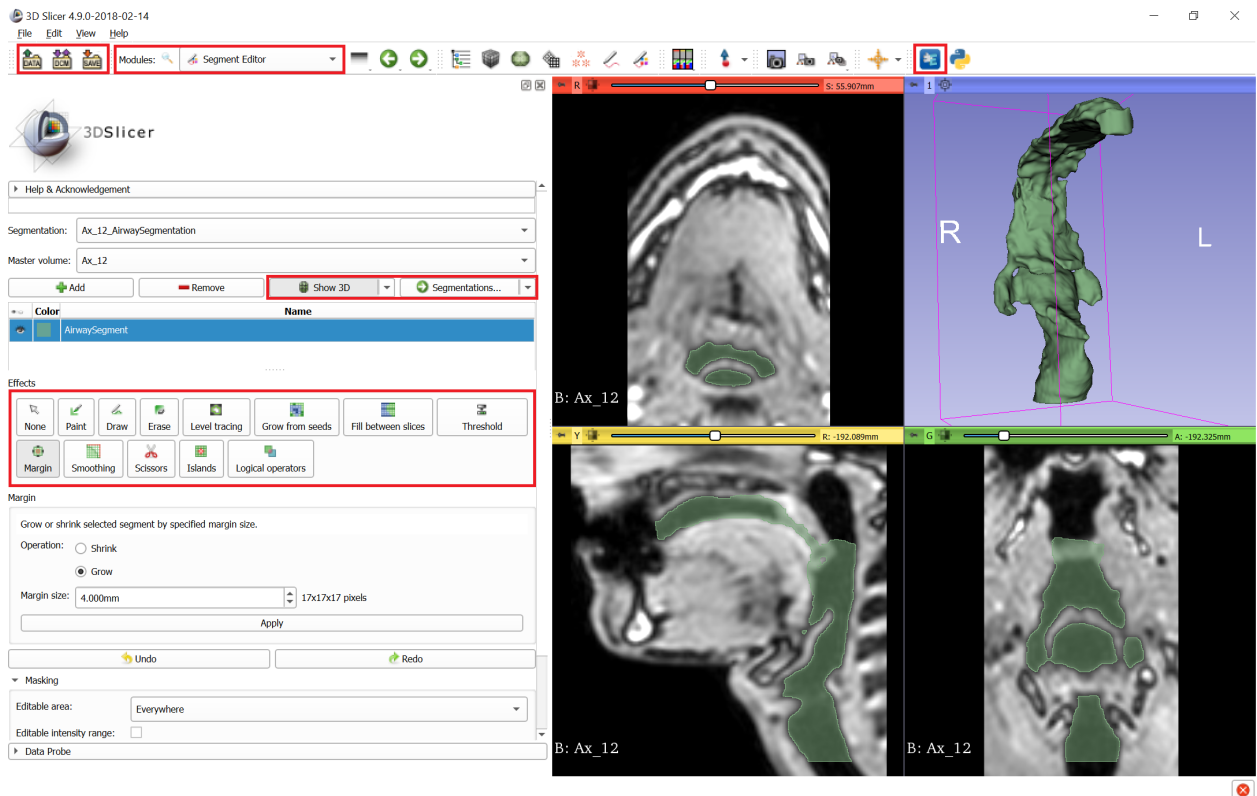


Figure 2.1: 3D Slicer User Interface. The current module, segment editor, is shown near the top left of the page, adjacent to the save and load options. On the right near the top is the extension manager which can provide additional segmentation tools. On the left, the effects that can be used in the segmentation process are shown, in addition to a toggle to show the 3D result of that segmentation. Finally, the lower right region shows the volume currently being used for segmentation in the orthogonal views and a 3D rendering of the segmentation. In this region, the selected voxels are colored and represent the region of interest as constructed using the module effects.

2.1.2 Mould Design

The two STL files obtained from 3D Slicer are imported into CAD software Rhinoceros 6 (<https://www.rhino3d.com/6>), the smaller of which is referred to as the inner lumen and the larger as the shell. These mesh files are first scaled to the desired size for experimental use and then converted to NURBS polysurfaces to allow them to be manipulated during the mould design process. As a result of the conversion, file size and processing time increase dramatically. To combat this, the mesh files are reduced to 20,000 elements before conversion to NURBS polysurfaces. This retained sufficient detail for rapid prototyping while reducing processing time.

Both polysurfaces have features added to them and slight shape alterations, specifically, around the inlet(s) and outlet(s). At these locations, the shape of the model can be irregular and not suitable for use in an experimental setup. As such, the inlet(s) and outlet(s) are trimmed and formed into a cylinder of specific diameter to facilitate easy connection to the experimental setup. The diameter of this cylinder is determined by the available fittings and the type of fit desired, for example, the cylinder could be placed around the outside of the fitting and then clamped onto it or it could be inserted inside a fitting and secured using a sealant.

The inner lumen is required to maintain its position inside the two mould halves. In order to achieve this, alignment dovetails are added to the end of the inlet(s) and outlet(s) as seen in figure 2.2. At this point, the inner lumen and shell are prepared for the next stage of the mould design.

Parting Line

The shell is made up of roughly 20,000 3 sided planar surfaces, of which a large amount need to be split in order to split the shell into two pieces; these two pieces form the basis for the two mould halves. In addition, the parting line has to be positioned such that in the pull direction, (the direction with which the two mould shells are taken apart after casting, see figure 2.3) there are none to minimal undercuts and wherever possible the size of the undercuts are reduced as they inhibit demoulding. Therefore, a pull direction has to be established which will achieve this outcome. It is important to note that all problems related to undercuts and demoulding can be solved by modifying only the shell geometry. Hence, it is very important to inspect and modify the shell in 3D Slicer prior to designing

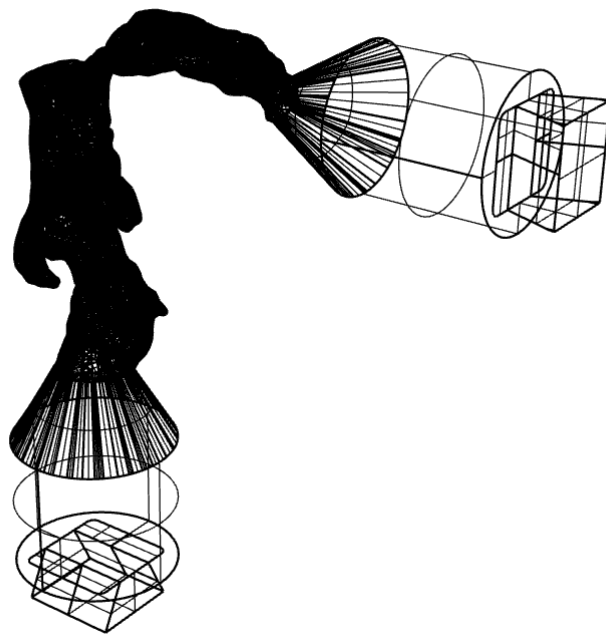


Figure 2.2: Prepared inner lumen with cylindrical inlet and outlet, in addition to alignment dovetails. The shell looks identical however, the cylinders are larger by the wall thickness of the phantom and it does not yet possess alignment dovetails. The inner lumen is one part of the three-part mould used to cast the silicone phantom.

the mould as this will make the design process easier. This is also beneficial as we do not have to modify the inner lumen geometry, meaning it will be left as physiologically accurate as possible. We should also note that the fluid flow is only affected by the inside geometry and the exterior geometry only affects the applied deformation.

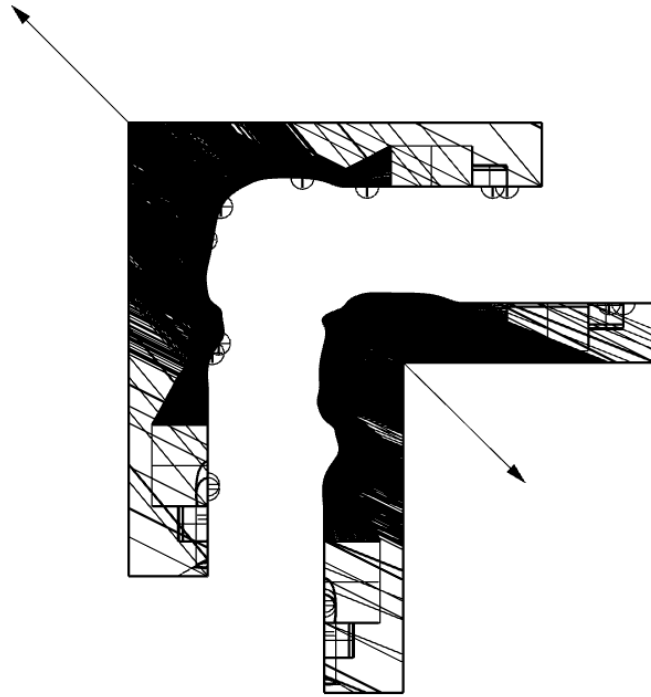
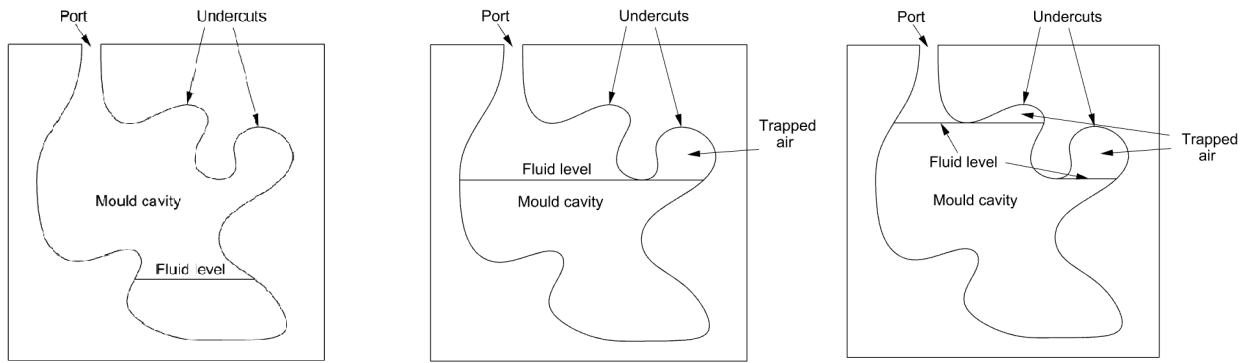


Figure 2.3: The pull direction is indicated by the arrows connected to each mould half. Each mould half can pull away from the other as there are no physical obstructions to prevent this from occurring.

Once a pull direction has been determined, we must then consider the orientation with which the mould will possess as it is filled. As with any fluid filling a container, air bubbles can be trapped due to density differences. To start with, the mould is completely filled with air, as silicone rubber is added, some air escapes the mould as it is replaced by the silicone. Some air bubbles remain in the mould as there is no path for them to take which will allow them to escape, hence they are trapped, see fig 2.4. These undercuts are resolved through a combination of changing the orientation of casting and adding escape routes for the air to take, see fig 2.4.

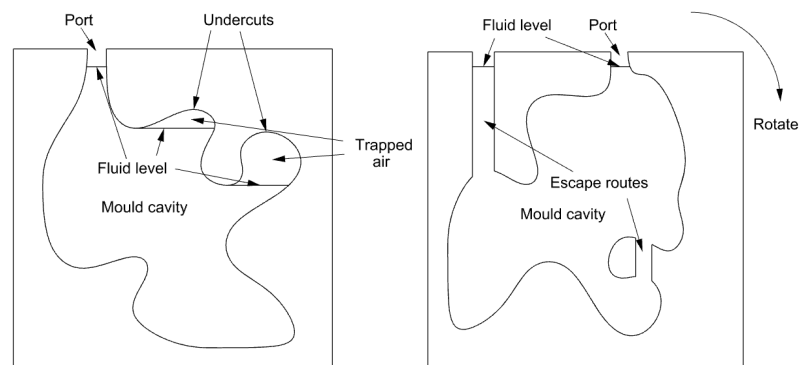
The parting line is then established along the surface of the shell by projecting a curve onto it from an orthogonal view which is perpendicular to the pull direction. This curve is created through numerous iterations and inspection to ensure that each mould half does not



(a) Mould partially filled.

(b) Mould filled to first undercut, air is now trapped in this undercut.

(c) Mould filled to the second undercut, air is now trapped in both the first and second undercuts.



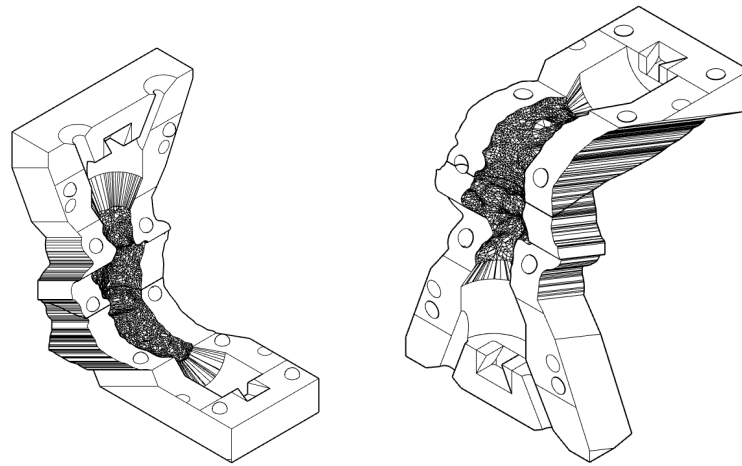
(d) Mould completely filled, air remains trapped in the two undercuts.

(e) To resolve the issue of undercuts, the mould can be rotated to change the orientation of casting and escape routes can be added.

Figure 2.4: A simulation of undercut formation in a single plane of an arbitrary mould as it is filled with a fluid.

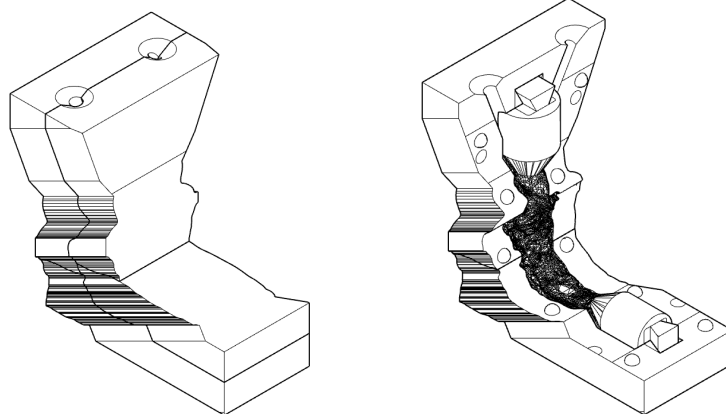
contain undercuts when in the casting orientation. However, this process does not produce a perfect split with zero undercuts. To combat this the mould orientation is adjusted during the casting process and will be described in detail in a later section. The parting line is then used to split the shell into two pieces forming the cavity for each mould half. A parting surface is then created from the curve used to split the shell and registration elements are added to this surface. The result is two surfaces which connect to each other and form a cavity in the shape of the shell. These surfaces are then enclosed to form two closed polysurfaces.

In order to facilitate the inner lumen alignment dovetails, the inner lumen is placed in the mould halves, as it would be during casting, and then subtracted from the mould halves, leaving behind the female dovetail joint, see figure 2.5. Finally, two ports are added to the mould halves to allow the mould to be filled and to provide air a route to escape the mould. They are placed such that the air is able to escape given the chosen orientation of casting.



(a) Mould half A.

(b) Mould half B.



(c) Both mould halves in casting orientation.

(d) Mould half A with inner lumen inserted.

Figure 2.5: All mould pieces after completing the design process. Note that this design has been updated and does not reflect the cast phantoms used for the results as they were cast using a previous mould design.

2.1.3 Mould Manufacture

The material used to manufacture the moulds needs to be readily available in a 1.75 millimeter diameter filament for use in common rapid prototyping devices. It also is required to have good flexibility to facilitate demoulding and to overcome undercuts, and finally, it is essential that it can be easily smoothed. These requirements presented a unique challenge given that the mould had an intricate geometry that will be difficult to machine, even if using a computer numerically controlled (CNC) machine. Therefore, a different approach that can be easily carried out in a laboratory environment is required.

Manufacturing the mould is done using rapid prototyping technologies, as the mould geometry is highly complex, and complexity will not incur additional costs with this method of manufacturing. However, post-processing is needed in order to produce a mould capable of producing an optically accessible phantom with a smooth surface. Furthermore, the mould halves have to be broken into four pieces in order eliminate the requirement for supports and to ensure they will fit within the rapid prototyping device's build area.

In order to rapid prototype the mould designed in CAD, it first has to be exported as a mesh. Mesh generation primarily involves determining the maximum edge size of each mesh element, in this case, each triangle. This set of planar triangles became a representation of the CAD design, hence a smaller maximum edge size will capture more detail along a curved surface. The largest edge size is kept very low in order to capture as much detail as the rapid prototyping device can produce, in this case, 0.1 millimeters.

The STL mesh files are loaded into software FlashPrint (<http://www.flashforge.com/flashprint/>) which generates a type of GCODE specific to Flashforge devices, such as the FlashForge Dreamer 3D printer used here. The Flashforge Dreamer used had a nozzle diameter of 0.4 millimeters and layer heights in the range of 50 to 250 micrometers. It is primarily these two settings which determine how accurately the mesh file will be represented. GCODE generation requires modification of a variety of settings in order to produce a print that is free of defects such as stringing (where extruded material oozes out of the printer nozzle and leaves strings attached to the outer surface), and holes in the print surface. These are resolved by increasing filament retraction and increasing the infill percentage respectively. A balance of print time and material usage is carried out in order to allow mould manufacturing in a timely manner, using as little filament as possible, as this increases the cost of the mould. For a cost breakdown of the rapid-prototyped mould see table 2.1.

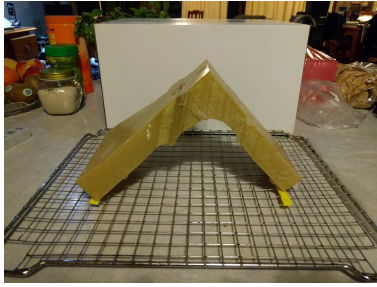
Table 2.1: Breakdown of the costs and time required to rapid prototype the mould used to cast the silicone phantom.

Item	Cost [\$]	Duration [hr]	Weight [g]
Mould Half A I	14.76	14.32	184.92
Mould Half B I	14.13	13.80	177.04
Mould Half A II Mould Half B II	6.08	6.50	76.24
Inner Lumen	5.92	7.00	74.22
TOTAL	40.89	41.62	512.42

Once the mould pieces are 3D printed, they require additional post-processing to improve the surface finish. First, the pieces are cleaned by hand using fine detail hand tools such as a scalpel and various tweezers. These tools remove any undesired material that is left behind by the printing process. This includes support material which is required for the inner lumen as it does not possess a flat surface to print from, and hence has numerous overhanging features. As a result, this piece of the mould is printed using a raft to increase bed adhesion.

The printing process creates a stepped surface finish, where each step has a height of the layer thickness. A rough surface finish on the mould creates a phantom with the same surface finish. As a result, the light passing through the phantom will be refracted irregularly and optical access will not be easily achievable due to its cloudy appearance. Furthermore, the flow structures will change due to this surface finish which is not found *in vivo*. To combat this, the surface finish is required to be as smooth as possible.

Various 3D printing materials are soluble in certain solutions. By using this knowledge, a vapor chamber is used to vaporise the solution with the 3D printed parts contained therein. Furthermore, every plastic has a temperature, known as its distortion temperature, whereby it becomes soft and malleable, but maintains its geometry and does not melt. By heating the vapor to the distortion temperature of the plastic used, the 3D printed part is easily smoothed in a matter of minutes, creating a smooth, glossy surface finish, see figure 2.6.



(a) Rapid-prototyped part prior to entering vapor chamber. Heatproof strips are placed between the part and the grate to prevent the part from melting.



(b) Vapor chamber placed over the rapid-prototyped part.



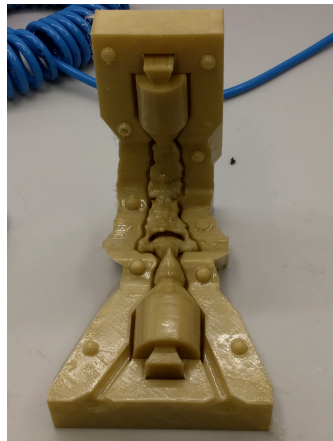
(c) Rapid-prototyped part and vapor chamber filled with vapor at the distortion temp, of the material used, for approximately four minutes depending on the desired level of surface finish.

Figure 2.6: Process of smoothing the rapid-prototyped parts using a vapor chamber filled with solvent and temperature maintained at the parts distortion temperature.

2.1.4 Model Casting

Using the method described previously by Corbett et. al. a silicone rubber phantom is cast and the method is revisited here [34]. The silicone rubber, Wacker Elastosil RT601 part A and B are combined in a beaker in a 9:1 ratio. This is mixed vigorously for 2 minutes whilst scrapping the sides of the beaker to ensure the proper combination of both components. It is then placed into a vacuum chamber at -90 kPa until all air bubbles created from mixing have risen out of the mixture, see figure 2.8. This typically takes 50 minutes however this can be accelerated by periodically letting air into the vacuum chamber to break the bubbles at the mixtures surface. Whilst waiting for the mixture to degas the mould is cleaned with compressed air and the inner lumen is placed into one of the mould halves. Its position is verified such that it produces a consistent wall thickness and is not touching the mould at any point other than at the alignment dovetails, see fig. 2.7. The wall thickness is relatively uniform as all mould pieces are rapid prototyped from the same material using the same hardware and software settings. Some inaccuracies are present in the wall thickness, which can be visually observed when the inner lumen is placed into one of the mould halves. This is not critical as it does not affect the flow as significantly as the shape of the inner phantom wall does.

The final mould half is then joined and the whole assembly is clamped together using 2 g-clamps and pieces of plywood to brace the mould. The mould is then clamped onto a vice which is able to rotate freely and lock in position. Initially the mould is placed at a 45-degree angle to the horizontal, however, this angle should be sufficient to allow air a path to escape the mould as it travels upwards; note that this angle will depend on the shape of the mould halves and can occur around 1 or 2 axes, see figure 2.9a. The mould angle is adjusted at various stages throughout filling until the mould is full, at which point it is in the horizontal position. In order to help air bubbles escape during filling the mould is vibrated with a rubber hammer before each angle change and after the mould is full for roughly 30 seconds to 1 minute. The mould is left to set overnight at room temperature as this gives more time for air bubbles to rise out of the mould.



(a) Mould half A.

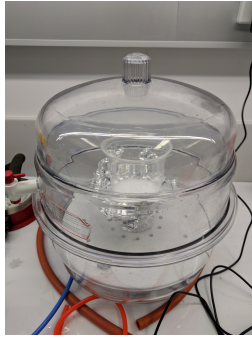


(b) Mould half B.

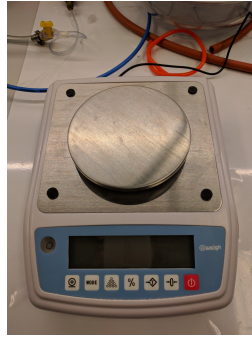
Figure 2.7: The inner lumen is placed inside each mould half prior to casting to verify its position with respects to the mould halves. As can be seen, the inner lumen does not touch the mould halves at any point along its length.

The clamps are removed and one mould half is carefully separated using a thin metal scraper to reveal the mould cavity and inner lumen. The inner lumen is then carefully removed from the remaining mould half as the silicone rubber is easily torn if caught in the mould. The result is a uniform wall thickness silicone phantom containing an inner lumen mould which needs to be removed.

In the same solution which is used to smooth the mould pieces, the inner lumen, including the silicone phantom is placed. Over time the inner lumen dissolves into the solution leaving behind only the silicone. The process of dissolving the inner lumen takes anywhere from 6



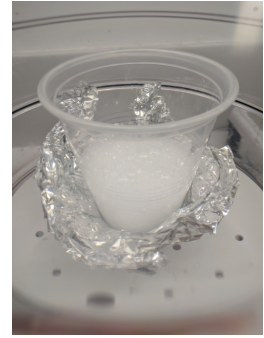
(a) Vacuum chamber.



(b) Weighing scale.



(c) Pressure gauge.



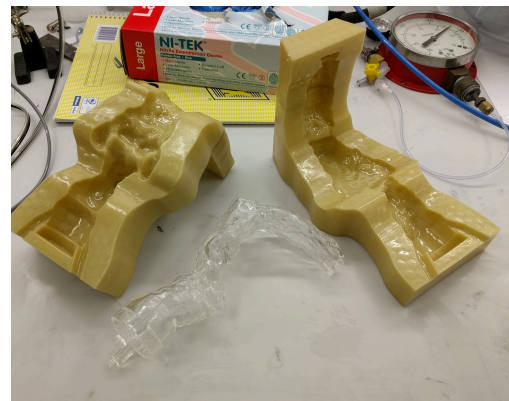
(d) Mixture prior to degassing.

Figure 2.8: The process of mixing and degassing the silicone rubber prior to casting.

hours to several days depending on a variety of factors. These include the temperature of the solution, agitation, the shape of the inner lumen and what percentage of the material is exposed to the solution. The final result is a usable silicone phantom, with uniform wall thickness, see figure 2.9b.



(a) The position of clamped mould immediately prior to casting.



(b) Silicone rubber phantom, casting artifacts such as the inlet and outlet ports and flashing are removed using a sharp Stanley blade.

Figure 2.9: Mould before and after casting.

2.2 Experimental Setup

The experiential setup consists of all the components required to simulate *in vivo* conditions, including the flow rate and wall deformation.

2.2.1 Flow Circuit

The flow circuit is made from the combination of a variety of fittings and components to facilitate the flow of fluid passing through the silicone phantom. This is required to allow the use of a working fluid other than air, that improves optical access by matching the refractive index of the phantom, hence allowing PIV measurements to be taken. See figure 2.10 for an overview of the flow circuit.

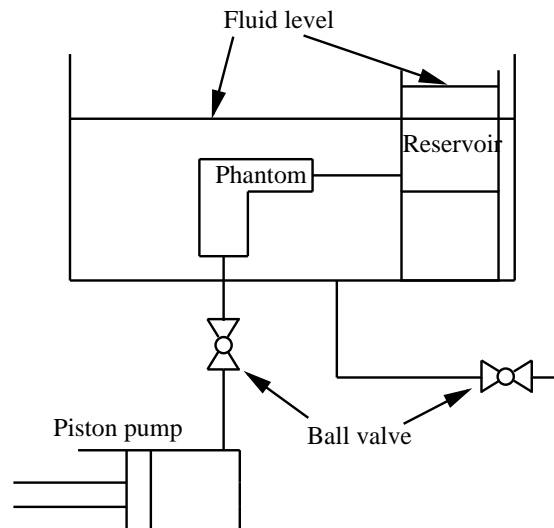


Figure 2.10: The piston pump provides oscillatory flow controlled by a stepper motor. The ball valve connected to the pump allows the pump to be isolated and drained when not in use. In addition, the second line containing a ball valve is used to drain the tank after use. The phantom is submerged in a tank and connected to the pump and reservoir, the fluid inside these areas contains tracer particles.

2.2.2 Piston Pump

To successfully simulate the flow through the phantom, a single cylinder piston pump is employed. The pump is positioned at the trachea end of the phantom as one end of a nonrecirculating flow circuit, creating expiration on the upward stroke and inspiration on

the downward stroke. The piston pump is manufactured using rapid prototyping and off the shelf components. This resulted in a cost-effective and reliable piece of hardware that is modular and highly customisable.

The piston is moved by a linear actuator with a specially designed core using the open source v-slot track by Open Builds (<https://openbuilds.com/>). The v-slot provides a means of fixing additional accessories in the future if required, and it can be used as a rail for linear motion. In addition to the core, the linear actuator is made up of four other components, a motor plate, end plate, rod with lead nut and lead screw with coupler, as seen in figure 2.11. As these parts are rapid-prototyped the rod and lead screw are combined with the lead nut and coupler respectively to reduce the component count, simplifying the design. The design of the lead nut and core components were influenced by open source project Maker Muscle, (<http://makermuscle.com/>) which used a similar t-slot track. Hardware for the piston pump is kept to a minimum by using tapped holes in the 3D printed parts to suit low profile M5 bolts and all components are designed to accommodate readily available NEMA type stepper motors. The linear actuator is bolted onto a 4040 t-slot aluminum extrusion to provide rigidity and further customisation, see figure 2.12 for an assembly of the linear actuator.

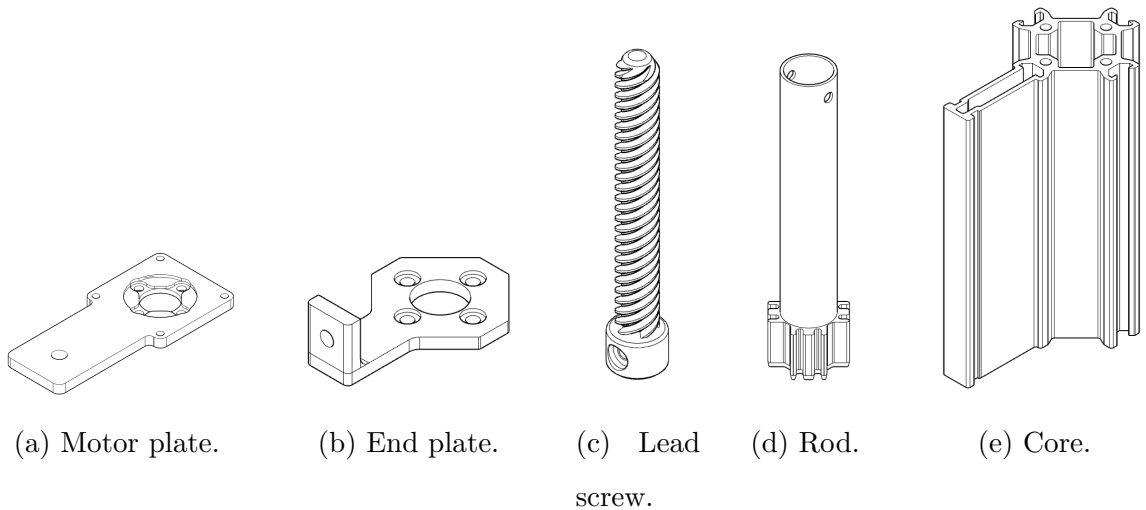


Figure 2.11: CAD drawings of the linear actuator components.

The piston head is designed with two grooves to suit 2.6162 millimeter nitrile rubber o-ring. Two grooves are needed to prevent the piston from moving in a non axial direction through the bore and also provides a backup seal if one fails. It is critical that the rubber is able to glide smoothly over the bore, hence a very smooth surface finish is required which

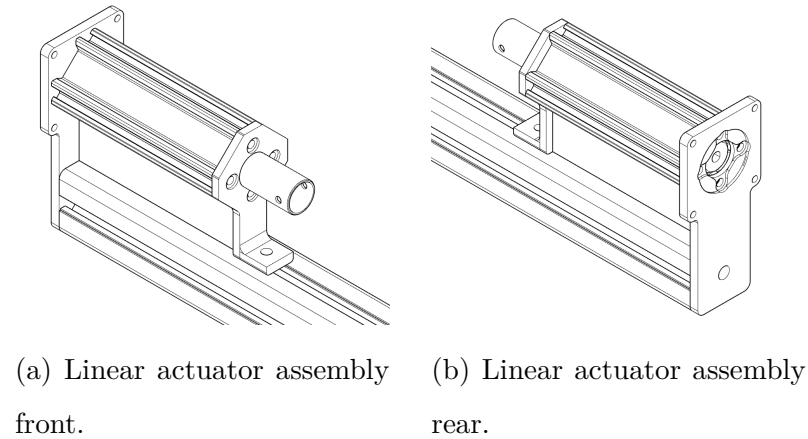


Figure 2.12: Linear actuator assembly in CAD.

rapid prototyping can not achieve. As such, PVC pipe is used since its surface finish is very smooth and is available in a large variety of sizes. Furthermore, lubricant HydroSeal is applied liberally throughout the walls of the pipe which ensures the piston can move freely with very little friction while remaining sealed. In order to determine the dimensions for the piston groove an analysis is carried out using available tables of data and sealing principles.

The piston head is attached to the rod of the linear actuator and the bore holders are rapid-prototyped to secure the bore to the t-slot aluminum extrusion. This ensures that all components are aligned along a single axis, as any misalignment will cause large amounts of friction and potentially break the piston pump, see figure 2.13 for the rapid prototype piston components and figure 2.14 for an assembly of the piston components and the linear actuator.

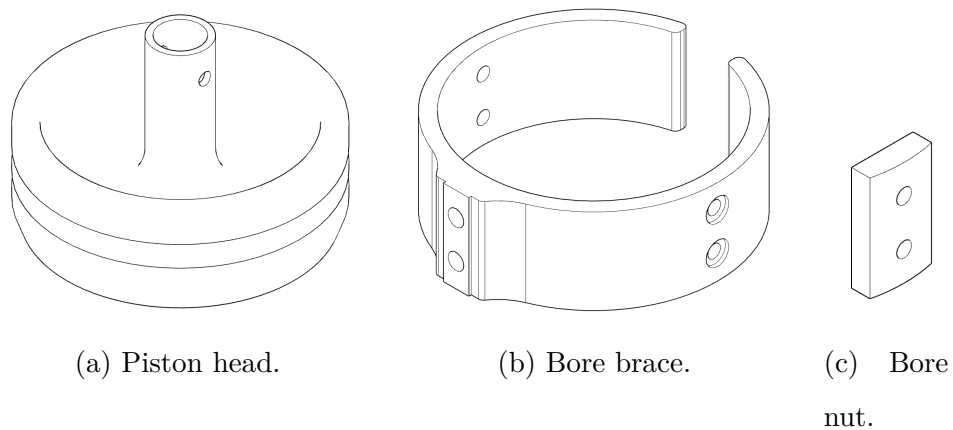


Figure 2.13: Piston components.

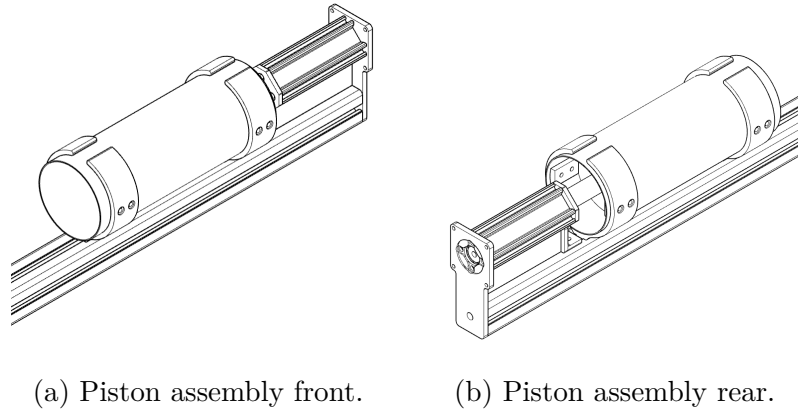


Figure 2.14: Piston pump assembly in CAD.

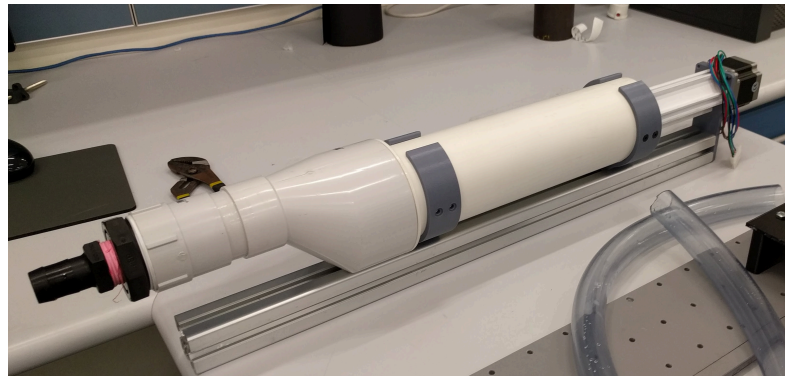


Figure 2.15: Piston pump setup, note that a reducer is added to the end of the bore in order to facilitate a 25 mm polytube for fixing to the remainder of the setup. All connections are either cemented using PVC cement or threaded with British Standard Pipe (BSP) fittings and Teflon tape. The polytube is fitted with a hose clamp.

2.2.3 Flow Rate

The working fluid moved by the piston pump is a mixture of water and glycerol. This is necessary due to the refractive index of the silicone rubber phantom to that of the surrounding fluid. Their values should be equal as light passing through the phantom is dispersed due to its complex geometry. As a result, the working fluid flow rate is Reynolds matched to that of the simulated working fluid at physiological flow rates. In this case, the flow rate is matched to that of air at $30L/min$. Furthermore, the phantom's size is altered, adjusting the flow rate further.

$$Re = \frac{v \times d}{\nu} \quad (2.1)$$

$$Re_1 = Re_2$$

$$\frac{v_1 \times d_1}{\nu_1} = \frac{v_2 \times d_2}{\nu_2} \quad (2.2)$$

$$v = \frac{\dot{Q}}{A} \quad (2.3)$$

$$(2.3) \rightarrow (2.2)$$

$$\frac{\dot{Q}_1 \times d_1}{A_1 \times \nu_1} = \frac{\dot{Q}_2 \times d_2}{A_2 \times \nu_2} \quad (2.4)$$

$$A_2 = s^2 \times A_1 \quad (2.5)$$

$$d_2 = s \times d_1 \quad (2.6)$$

$$(2.6), (2.5) \rightarrow (2.4)$$

$$\begin{aligned} \frac{\dot{Q}_1 \times d_1}{A_1 \times \nu_1} &= \frac{\dot{Q}_2 \times s \times d_1}{s^2 \times A_1 \times \nu_2} \\ \dot{Q}_2 &= \frac{\dot{Q}_1 \times \nu_2 \times s}{\nu_1} \end{aligned} \quad (2.7)$$

Using equation (2.7) it is determined that a flow rate of $15.81 \frac{L}{min}$ is required to simulate *in vivo* conditions when using a water-glycerol mixture with a ratio of 1:1, which is roughly the required ratio to achieve the correct refractive index for optical clarity [36].

To determine the diameter of the piston head, an analysis is carried out considering the Reynolds matched flow rate and max achievable velocity of the piston head. Using the bore diameter of a commonly available PVC pressure pipe as input for the calculations.

$$v = \frac{\dot{Q}}{\frac{\pi}{4} \times d^2} \quad (2.8)$$

In order to achieve the required flow rate, the piston head needs to move at the calculated velocity. This velocity is achieved through a combination of varying the bore diameter, adjusting the lead on the actuator lead screw, and through motor selection to drive the actuator.

To control the flow rate of the working fluid passing through the phantom the lead screw of the piston pump is attached to a NEMA 23 stepper motor. The stepper motor rotates 1.8 degrees per step and can be microstepped to reduce this value further providing a smooth flow profile and increasing accuracy. Hence, the step rate is determined based on the specifications of the hardware and the desired flow rate see equation (2.13).

$$\begin{aligned} \dot{Q} &= \frac{Q}{t} \\ \dot{Q} &= A \times \frac{d}{t} \\ v &= \frac{\dot{Q}}{A} \end{aligned} \quad (2.9)$$

$$v = \omega \times l \quad (2.10)$$

$$(2.9) = (2.10)$$

$$\begin{aligned} \omega \times l &= \frac{\dot{Q}}{A} \\ \omega &= \frac{\dot{Q} \times l}{A} \end{aligned} \quad (2.11)$$

$$sps = \omega \times spr \quad (2.12)$$

$$(2.11) \rightarrow (2.12)$$

$$sps = \frac{\dot{Q} \times l}{A} \times spr \quad (2.13)$$

Where sps is the steps per second, spr is the steps per revolution, as determined by the stepper motor and the degree of microstepping, and l is the lead.

The flow rate desired needs to match a sine wave, hence the value for \dot{Q} is described as $\dot{Q} = A \times \sin(B \times t + C) + D$ and the values for A, B, C, D are adjusted according to the

magnitude, period of oscillation, x-axis offset and y-axis offset respectively.

An accelerometer was placed on the shaft of the linear actuator to ensure that the acceleration values of the actuator matched the sine wave provided to the control system and produced the desired flow rate. Furthermore, a reservoir was connected to the piston pump outlet and filled with water. The water level was measured as the pump oscillated and this data was used to experimentally validate the flow rate of the pump against its input.

2.2.4 Phantom Deformation

To enable the investigation of fluid structure flow interaction the wall of the phantom is required to be deformed in a controlled way, that matches the deformation observed *in vivo*. To achieved this a set of linear actuators are used by positioning them at a point of interest along the phantom. This enables the wall to be deformed at the location of the actuator, hence, it is essential to have a system that allows the actuators to move with respects to the phantom such that deformation can be applied to any point of interest.

A rail system is rapid-prototyped using an aluminum t-slot extrusion and M5 and M6 mounting hardware to allow movement of the actuator in three axes.

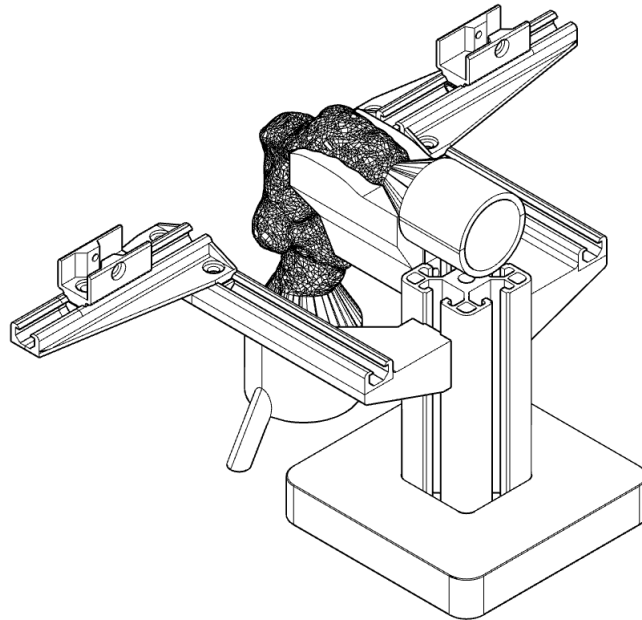


Figure 2.16: Actuator rail system to suit two Actuonix L12 actuators for use in deforming the phantom.

One case of deformation was considered, the deformation experienced by the airway

matches that of the third set of arrows in figure 1.2. That is, a slight movement of the vertical section of the airway in a posterior motion.

2.2.5 Electronics Control

In order to control the motor and actuators, an electronic circuit is developed. An A4988 stepper driver with current limiting is used to drive the NEMA 23 bipolar 6 wire stepper motor. The current limiting allows the motor to run at higher than rated voltages, hence achieving faster step rates. Two Actuatorix L12 actuators, along with the motor, are connected to a breadboard supplied with 5 volts from an Arduino and 24 volts from a power supply unit (PSU). The 5 volt line is used as a logic circuit to control the actuators and the motor. The 24 volts line is used to power the motor and actuators which are rated at 12 volts, 1 amp and 6 volts, 0.46 amps respectively. The PSU is able to supply 4.5 amps at 24 volts, this is sufficient for the two actuators and the motor, however, the voltage needs to be adjusted. As a result, an LM317 voltage regulator along with two potentiometers are used to adjust the output voltage to the rated voltage for each component.

Jumper wires are used to connect all components together and a case is rapid-prototyped to house all electrical components. Furthermore, a case for the PSU is designed and rapid-prototyped, having a C14 plug for mains connection, two banana plugs for the positive and negative terminals of the PSU and a light up rocket switch. This eliminates the possibility of accidentally coming into contact with mains voltage or creating a short circuit.

2.2.6 Tank

The tank is manufactured using high optical clarity glass on all sides which will require optical access. The remaining sides are constructed using cell cast acrylic to reduce costs. The tank is put together using silicone and holes are drilled into the shorter set of parallel sides and the bottom panels of the tank. These holes are used as inlets and outlets for the flow circuit, in addition to providing flexibility to change the setup configuration. Furthermore, one hole is reserved to drain the tank if required.

The tank is plumbed using commonly available pressure pipe and BSP fittings. Each hole is fitted with either a BSP bulk head or a rapid-prototyped plug which is sealed to the glass using a rubber ring or silicone respectively. The bulk heads provided more modularity

as they can be changed very quickly compared to the silicone plugs as the silicone needs to be removed and reapplied, then allowed to cure.

The tank needs to be raised to allow access from the bottom panel and to provide clearance for the fittings. Hence, a stand is manufactured using t-slot aluminum extrusions. The stand allows the tank to move axially along it, assisting with the positioning of the tank during result collection. This is achieved through the use of linear rails bolted to the stand.

Once sealed and plumbed the tank is filled with a solution of water and glycerol. To determine the ratio, a phantom is placed in the tank, the tank is then filled to halfway of its final height with glycerol. Water is added slowly and mixed with the glycerol until the phantom becomes invisible to the naked eye. A grid is placed on one panel of the tank and observed as water is added. This assisted in the process as the grid lines start curved but become straight and regular when the correct amount of water is added.

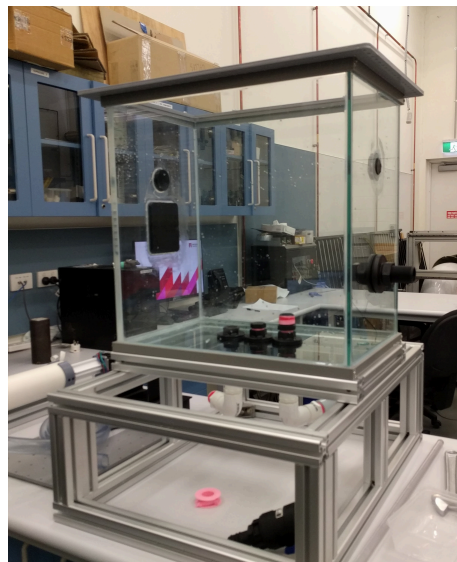


Figure 2.17: Tank and t-slot stand with flow circuit connections on the bottom panel and sealed plugs on the side panels.

2.2.7 Phantom

The phantom is connected to a bulk head located on the bottom panel of the tank through the use of a union. The union provides a quick, sealed connection allowing the phantom to be swapped out. The remaining end of the phantom is similarly connected via the use of a union to a reservoir inside the tank. The phantom therefore makes a sealed circuit relative to the tank. This is necessary as tracer particles are placed inside the fluid, and having a

smaller volume of fluid allowed for fewer particles to be used and eliminated incorrect results influenced by tracer particles in the tank.

The tracer particles used are glass spheres, having an average particles size in the range of 9 to 13 micrometers, and a density in the range of 1.05 to 1.15 grams per milliliter. This density is suitable as it is very close to that of the fluid mixture, hence the buoyant and gravitation forces cancel out and the particles velocity is only affected by the forces it experiences in the fluid flow.

2.3 PIV Setup

A synchroniser connected to a high speed camera and laser, captures image pairs of tracer particles moving through the phantom. In order to achieve this the setup first needs to be calibrated. A laser sheet is produced through the use of a periscope connected to the output of the laser. The periscope is then positioned above the tank, producing a laser sheet through the tank. To align the laser sheet with the region of interest, the tank is moved along the frame using the attached linear rails then locked into position.

The camera is then set up on a tripod next to the tank pointing horizontally towards the region of interest. Prior to installing the phantom to the tank, an alignment sheet is used to focus the camera on the laser sheet. An image pair, known as the calibration image is taken using software Synchroniser Control. A known distance on the image is then provided to the software, in addition to a pulse delay between image pairs. The pulse delay is determined by the estimated velocity of flow inside the region of interest given by its area and the flow rate of the pump.

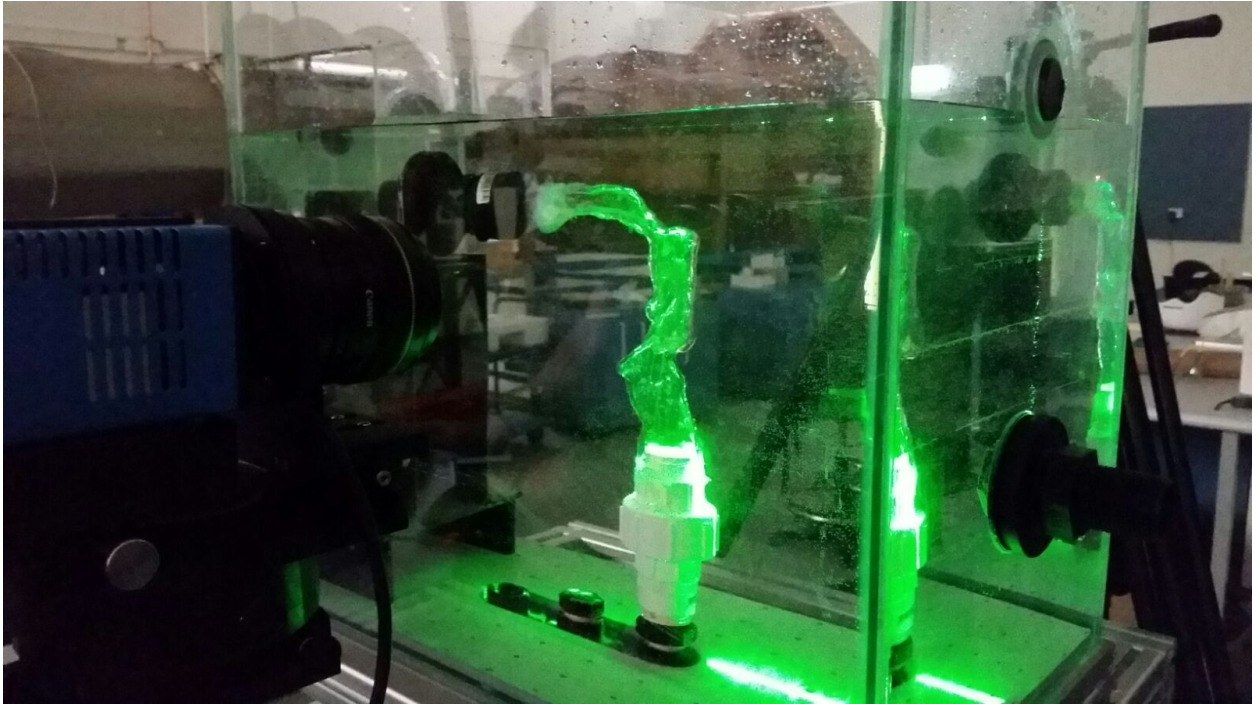


Figure 2.18: Phantom in the tank with water-glycerol mixture. PIV equipment setup with laser sheet in the sagittal plane and camera pointing perpendicularly to the sheet.

2.4 Computational Fluid Dynamics

The model used to perform simulations upon is reconstructed using the process described in section 2.1.1 and is identical to the silicone phantom. The simulation is run with software Ansys 18.2 Academic version. A steady state CFX simulation is carried out using the parameters presented below.

- Steady state flow.
- Incompressible air at 25 degrees Celsius.
- Turbulence model BSL Reynolds stress.
- No slip boundary condition for the walls of the model.
- Inlet boundary at the mouth.
- Outlet boundary at the start of the trachea.

It should be noted that this simulation was isothermal, however, air traveling through the airway is heated during inspiration.

A mesh independence study is carried out to eliminate the error due to mesh generation. It is observed that the velocity and pressure experienced a change of less than 5 percent between the two final meshes each having an element count of 6.6 million and 28.7 million.

Chapter 3

Results

3.1 Particle Imaging Velocimetry

The PIV system was used to collect preliminary results. Figure 3.1 presents a plot of instantaneous velocity vectors in the sagittal plane during inspiration. The region starts at the back of mouth near the uvula and ends immediately after the epiglottis. It can be seen that the fluid flows down from the uvula along the anterior wall. This flow moves down and diverges, with the majority entering the epiglottis and the minority continuing down the remainder of the pharynx and towards the trachea. The experimental results for the flow field included velocity vectors lying outside the region of interest. Hence, a mask was applied during post processing and does not exactly match the shape of the model used in CFD.

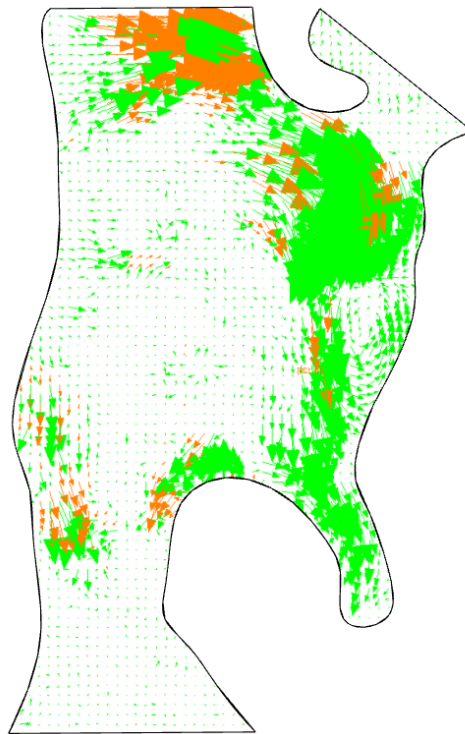


Figure 3.1: Velocity vector profile in the sagittal plane with constant inspiratory flow rate. The vector size indicates the magnitude of the velocity. The uvula and epiglottis can be seen at the top right and bottom right of the figure respectively. The outline was created through the use of a mask and is an indication of the phantom wall.

3.2 Computation Fluid Dynamics

Results in figure 3.2 show the flow field obtained from the computational model using a Reynolds matched inlet flow condition similar to the experimental. By comparing the direction of the velocity vectors, matching patterns can be observed at the anterior wall of the upper airway model but not in the central region. The pattern of flow distribution at a region adjacent to the epiglottis, entering into the tracheal is also similar to what has been obtained in the experiments. While a detailed flow field has not been obtained from the experimental models, the following results obtained using the computational model provide insights into the flow field distribution at multiple axial sections of the upper airway model, see figure 3.3. At the section of the uvula, velocity magnitude is high around the uvula structure and towards the posterior wall and this is likely due to the fact that the flow was coming from the oral cavity. At the section between the uvula and epiglottis, velocity magnitude appears to be high at the anterior and posterior walls with some flow still influenced by the tail end of the uvula structure. At the section of the epiglottis, the flow velocity is high at the posterior wall and as described in the previous section, such observation is less obvious in the experimental model. The velocity field distribution appears to be more distributed after the epiglottis downstream and at levels closer to the trachea.

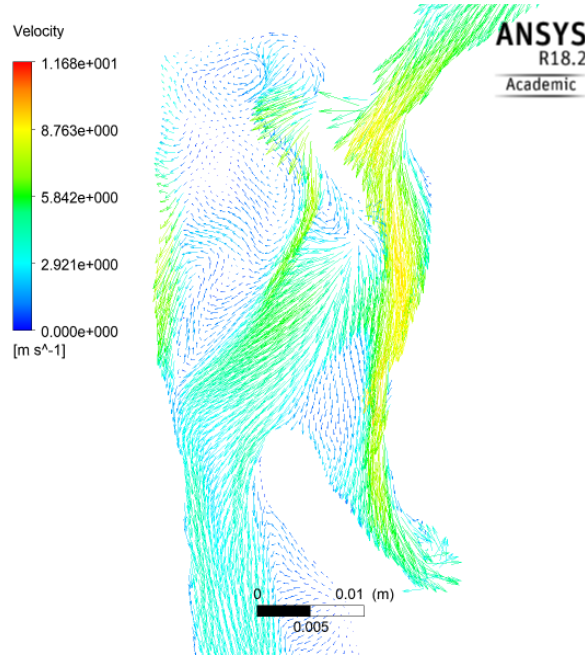


Figure 3.2: Velocity vector profile in sagittal plane with a flow rate of $30 \frac{L}{min}$ of air.

The velocity distribution flow profile and the corresponding pressure profile in the mid

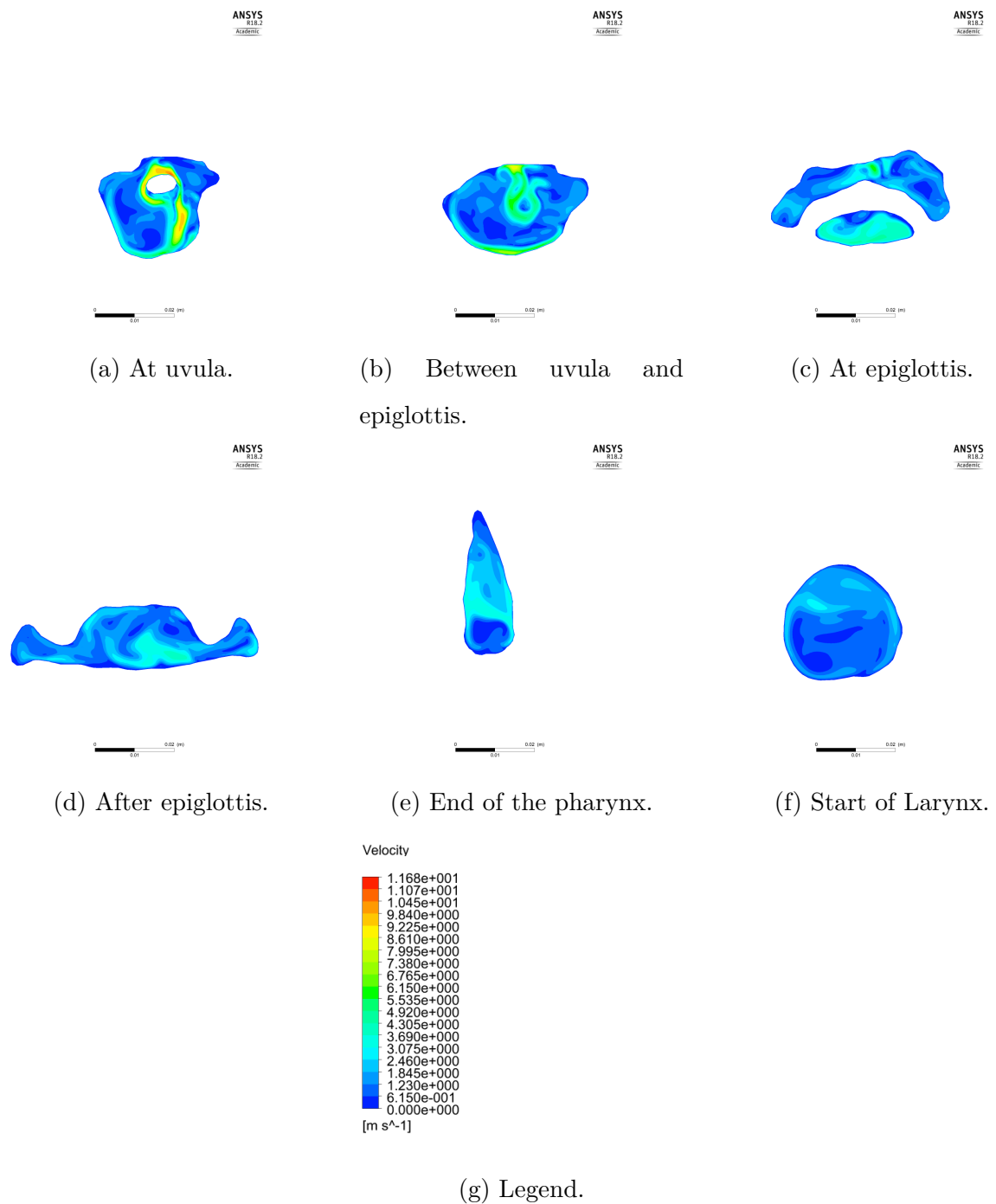
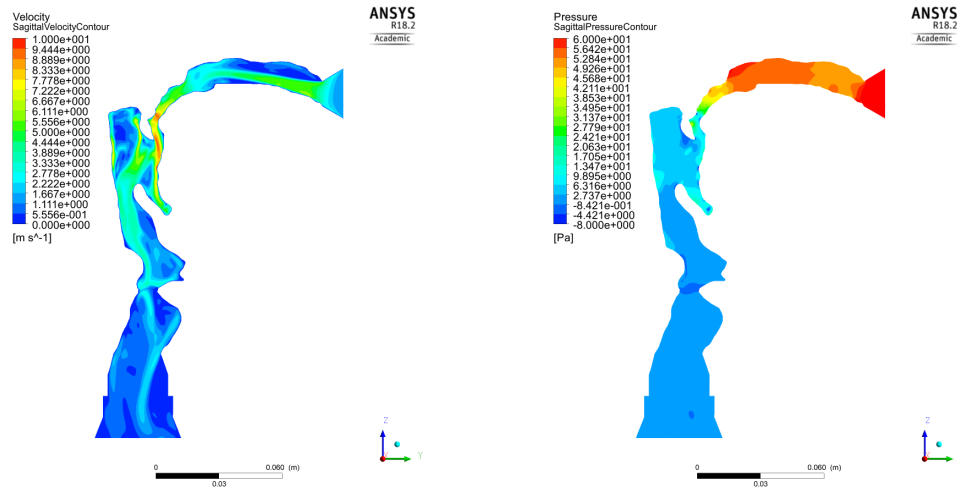


Figure 3.3: Velocity contours in the axial plane from CFD simulations with a flow rate of $30 \frac{L}{min}$ of air at various points along the length of the pharynx.

sagittal plane are shown in figure 3.4. Results show that pressure is high at the mouth leading to the upper airway with a dramatic change in pressure at the uvula.



(a) Velocity contour.

(b) Pressure contour.

Figure 3.4: Velocity and Pressure contours in the sagittal plane from CFD simulations with a flow rate of $30 \frac{L}{min}$ of air.

Chapter 4

Discussion And Future Work

4.1 Discussion

Problems related to fluid structure flow interaction can be found throughout biological systems. Biological flow processes such as blood flow in blood vessels, cerebrospinal fluid flow along the spinal canal and the flow of aqueous humor from the eye anterior chamber to the suprachroidal space are highly complex and research over the past decade has consistently demonstrated that disruptions to healthy flow is the major precursor for diseases such as aneurysm, syringomyelia and glaucoma. The advancement in computer technology and numerical methods has enabled computational fluid dynamics (CFD) to emerge as a common tool to study complex flow phenomenon but it is important to understand that results from numerical modeling need to be thoroughly validated by experiments especially since the boundary conditions presented in a biological problem are highly complex, which includes transient flow and moving wall boundaries.

While there is a plethora of studies on respiratory flow modelling, very few experimental work has been conducted to validate results of the models. More importantly, in existing experimental studies, silicone replicas of the human respiratory tracts have been developed and used but it remains unclear whether they are sufficient to reproduce the realistic physiological flow process in the airways since they are usually overly simplified. For example, the bulk soft tissues that surrounds the airway is represented by a silicone membrane with mechanical properties that are not matched with the actual soft tissues and in the case of the upper airway, moving wall boundaries from the activation of respiratory muscles during respiration has never been inclusively modeled.

The determination of inhalation flow profile experimentally in the human upper airway has been undertaken through the development of a PIV system. The flow profile appears to match the results of a computational model with similar inlet flow conditions at specific regions of the upper airway and there are some discrepancies at the airway center and below the uvula. The reasons for this are unclear and may be related to the deformation of the uvula or deformable airway walls which may have resulted in the loss of fluid energy as it flows pass the structure. Such an observation, if true, may present wide implications to the existing modeling efforts in predicting drug deposition using computational models as it suggests that rigid walls may not be appropriate in these simulations. Nevertheless, it is important to note that even though both the experimental model and the computational model are developed using the same set of MRI anatomical images, there appears to be some difference in the geometry presented in the Results. The reason for this is because of the mask applied over the image output from the PIV experiment. This image contains a sagittal view of the cast airway, hence, it is difficult to isolate the sagittal plane where results were taken as a silhouette of the airway is presented.

Another observation in the experimental study is that the flow at the anterior wall of the upper airway appears to be driven into the epiglottis structure. Given that this is likely to influence and entrain the transportation of fine particles, drugs deposited and trapped at the epiglottis are unlikely to be transported further downstream. However, it is important to note that predicting accurate drug transportation and deposition by observing streamlines and velocity vectors in the upper airway is not possible and detailed studies will need to be conducted to verify these speculations.

The PIV system and the accessories have been proven to work well. The pump which has been developed to deliver a pulsatile flow has operated effectively without any leakage in the device. As mentioned, it is important to note that the pump has been designed to be simple in construction and consists of parts that can be easily replaced through rapid-prototyping. Further modifications to improve the stroke of the pump to deliver a faster flow rate can be easily accomplished by changing the stepper motor or adjusting the code. The connections of the upper airway organ to the tank have also been made simple through the use of standard fittings and this helps to reduce the setup time for the PIV system. It is important to note that although some flow induced motion of the upper airway was expected using the proposed connection, none or only very small motion was observed on the upper airway as

the liquid was pumped through the system. This shows that the existing way of connecting the organ was stable and reliable and is unlikely to influence the PIV measurements. The frame which the PIV tank rests on has also been designed to help initialize the alignment of the laser sheet by enabling the tank to slide to the desired locations during setup and this feature has also been proven to work well. One of the most complex tasks undertaken in this research, which is the development of an optically accessible airway model, has also been successfully achieved. However, there are some comments regarding the experimental setup that should be examined here as they have the potential to influence the experimental results.

Smoothing of the mould pieces using vapor changes the dimensions of each mould piece. The change in dimensions is largely due to the hygroscopic properties of the material used. During the smoothing process, the mould pieces absorb a large amount of water and as a result they swell. After smoothing, this water slowly diffuses into the atmosphere, usually taking one to two days before reaching equilibrium and original dimensions. It should be noted that their dimensions were not verified. Furthermore, the smoothing process reduces the distance between the high and low points (steps). Each step is defined by the manufacturing process and hence the difference in dimensions cannot exceed 50 to 100 micrometers.

Figure 2.18, shows the refractive index of the phantom in a solution of water and glycerol, however the ratio of water to glycerol was high as insufficient glycerol was available to fill the entire tank. Prior to filling the tank, the phantom was placed into a smaller acrylic container with a suitable ratio of water to glycerol such that the refractive index of the phantom and the solution were very closely matched, turning the phantom invisible to the naked eye.

4.2 Future Work

Due to time constraints, more repetition of the PIV study was not possible and existing work to repeat the measurements is currently in progress. In order to provide an improved measurement of the flow field, the percentage of glycerol in the tank has also been increased and this has helped to better match the refractive index with the silicone material that has been used to cast the upper airway. While the effects of a non-rigid wall on upper airway flow field presents an interesting problem, further work to characterize how boundary wall motion from the activation and deformation of the surrounding tongue muscles influence the

flow characteristic would be interesting and will be an objective of the future study.

Womersley's number was looked at however due to the lack of time, the period of oscillation was kept at something more-close to that found physiologically. When matching the Womersley's number, it was noted that the period of oscillation increased significantly, hence a longer stroke on the piston pump would have been necessary but this was unavailable at the time. Future work will ascertain that both the Womersley and Reynolds number are matched.

Additional work which will be proposed using the PIV system developed is to study the difference in the flow field between the upper airway of children and adults, as dramatic differences in upper airway geometry exist between them. Understanding the flow field in the aforementioned upper airways using experimental models will not only help to validate existing modeling work, but will also enhance our knowledge on the mechanisms of drug particles transport in these two groups of humans which will pave the way to enable more effective drug delivery devices to be designed and developed.

The PIV system is not only limited to airway models. It can be used to investigate the flow fields present in various aneurysms such as abdominal aortic aneurysms, aneurysms present in the circle of Willis and popliteal aneurysms. Furthermore, it can simulate the various biological fluid flows present in the human body and can provide insight on how their altering can influence the conduits that contain them.

References

- [1] M. Kryger, T. Roth, and W. Dement, *Principles and Practice of Sleep Medicine*. 4th ed. Elsevier, 2005.
- [2] A. Kourmatzis, S. Cheng, and H.-K. Chan, “Airway geometry, airway flow, and particle measurement methods: implications on pulmonary drug delivery,” *Expert opinion on drug delivery*, vol. 15, no. 3, pp. 271–282, 2018.
- [3] N.-C. Liu, D. R. Sargan, V. J. Adams, and J. F. Ladlow, “Characterisation of brachycephalic obstructive airway syndrome in french bulldogs using whole-body barometric plethysmography,” *PloS one*, vol. 10, no. 6, p. e0130741, 2015.
- [4] S. Cheng, E. C. Brown, A. Hatt, J. E. Butler, S. C. Gandevia, and L. E. Bilston, “Healthy humans with a narrow upper airway maintain patency during quiet breathing by dilating the airway during inspiration,” *The Journal of physiology*, vol. 592, no. 21, pp. 4763–4774, 2014.
- [5] C. Spence, N. Buchmann, M. Jermy, and S. Moore, “Stereoscopic piv measurements of flow in the nasal cavity with high flow therapy,” *Experiments in fluids*, vol. 50, no. 4, pp. 1005–1017, 2011.
- [6] S. B. Khatri and O. C. Ioachimescu, “The intersection of obstructive lung disease and sleep apnea,” *Cleve Clin J Med*, vol. 83, no. 2, pp. 127–140, 2016.
- [7] J. A. Wedzicha and T. A. Seemungal, “COPD exacerbations: defining their cause and prevention,” *The Lancet*, vol. 370, no. 9589, pp. 786–796, 2007.
- [8] R. J. Barrios, F. Kheradmand, L. K. Batts, and D. B. Corry, “Asthma: pathology and pathophysiology,” *Archives of pathology & laboratory medicine*, vol. 130, no. 4, pp. 447–451, 2006.
- [9] J. A. Dempsey, S. C. Veasey, B. J. Morgan, and C. P. O’Donnell, “Pathophysiology of sleep apnea,” *Physiological reviews*, vol. 90, no. 1, pp. 47–112, 2010.
- [10] I. Almendros, A. Carreras, J. Ramírez, J. M. Montserrat, D. Navajas, and R. Farré, “Upper airway collapse and reopening induce inflammation in a sleep apnoea model,” *European Respiratory Journal*, vol. 32, no. 2, pp. 399–404, 2008.
- [11] S. Cheng, J. E. Butler, S. C. Gandevia, and L. E. Bilston, “Movement of the human upper airway during inspiration with and without inspiratory resistive loading,” *Journal of Applied Physiology*, vol. 110, no. 1, pp. 69–75, 2010.
- [12] S. Cheng, J. Butler, S. Gandevia, and L. Bilston, “Movement of the tongue during normal breathing in awake healthy humans,” *The Journal of physiology*, vol. 586, no. 17, pp. 4283–4294, 2008.

- [13] N. A. Baertsch and T. L. Baker-Herman, "Inactivity-induced phrenic and hypoglossal motor facilitation are differentially expressed following intermittent vs. sustained neural apnea," *Journal of applied physiology*, vol. 114, no. 10, pp. 1388–1395, 2013.
- [14] V. J. Wedeen, T. G. Reese, V. J. Napadow, and R. J. Gilbert, "Demonstration of primary and secondary muscle fiber architecture of the bovine tongue by diffusion tensor magnetic resonance imaging," *Biophysical Journal*, vol. 80, no. 2, pp. 1024–1028, 2001.
- [15] W. M. Kier and K. K. Smith, "Tongues, tentacles and trunks: the biomechanics of movement in muscular-hydrostats," *Zoological journal of the Linnean Society*, vol. 83, no. 4, pp. 307–324, 1985.
- [16] A. Sokoloff and T. Burkholder, "Tongue structure and function," in *Craniofacial Muscles*. Springer, 2012, pp. 207–227.
- [17] S. Idris, A. M. Mlynarek, K. Ansari, J. R. Harris, N. Rizk, D. Cote, D. A. O'Connell, H. Allen, P. Dziegielewski, and H. Seikaly, "Multi-dimensional analysis of oral cavity and oropharyngeal defects following cancer extirpation surgery, a cadaveric study," *Journal of Otolaryngology-Head & Neck Surgery*, vol. 47, no. 1, p. 27, 2018.
- [18] S. Podvinec, "The physiology and pathology of the soft palate," *The Journal of Laryngology & Otology*, vol. 66, no. 9, pp. 452–461, 1952.
- [19] Y. Finkelstein, A. Meshorer, Y. P. Talmi, Y. Zohar, J. Brenner, and R. Gal, "The riddle of the uvula," *Otolaryngology—Head and Neck Surgery*, vol. 107, no. 3, pp. 444–450, 1992.
- [20] G. Back, S. Nadig, S. Uppal, and A. Coatesworth, "Why do we have a uvula?: literature review and a new theory," *Clinical Otolaryngology*, vol. 29, no. 6, pp. 689–693, 2004.
- [21] A. Malhotra and D. P. White, "Obstructive sleep apnoea," *The lancet*, vol. 360, no. 9328, pp. 237–245, 2002.
- [22] B. A. Senior, L. Rosenthal, A. Lumley, R. Gerhardstein, and R. Day, "Efficacy of uvulopalatopharyngoplasty in unselected patients with mild obstructive sleep apnea," *Otolaryngology—Head and Neck Surgery*, vol. 123, no. 3, pp. 179–182, 2000.
- [23] I. E. K. Trindade, A. d. O. C. Gomes, A. C. M. Sampaio-Teixeira, and S. H. K. Trindade, "Adult nasal volumes assessed by acoustic rhinometry," *Brazilian journal of otorhinolaryngology*, vol. 73, no. 1, pp. 32–39, 2007.
- [24] R. K. Mittal, D. F. Rochester, and R. W. McCallum, "Electrical and mechanical activity in the human lower esophageal sphincter during diaphragmatic contraction." *The Journal of clinical investigation*, vol. 81, no. 4, pp. 1182–1189, 1988.
- [25] P. M. Suratt, P. Dee, R. L. Atkinson, P. Armstrong, and S. C. Wilhoit, "Fluoroscopic and computed tomographic features of the pharyngeal airway in obstructive sleep apnea," *American Review of Respiratory Disease*, vol. 127, no. 4, pp. 487–492, 1983.
- [26] C. Guilleminault, M. W. Hill, F. B. Simmons, and W. C. Dement, "Obstructive sleep apnea: electromyographic and fiberoptic studies," *Experimental neurology*, vol. 62, no. 1, pp. 48–67, 1978.
- [27] R. B. Fogel, A. Malhotra, G. Pillar, J. K. Edwards, J. Beauregard, S. A. Shea, and D. P. White, "Genioglossal activation in patients with obstructive sleep apnea versus control subjects: mechanisms of muscle control," *American journal of respiratory and critical care medicine*, vol. 164, no. 11, pp. 2025–2030, 2001.

- [28] E. Sauerland and R. Harper, "The human tongue during sleep: electromyographic activity of the genioglossus muscle," *Experimental neurology*, vol. 51, no. 1, pp. 160–170, 1976.
- [29] E. S. Katz and D. P. White, "Genioglossus activity during sleep in normal control subjects and children with obstructive sleep apnea," *American journal of respiratory and critical care medicine*, vol. 170, no. 5, pp. 553–560, 2004.
- [30] L. J. Pittman and E. F. Bailey, "Genioglossus and intrinsic electromyographic activities in impeded and unimpeded protrusion tasks," *Journal of neurophysiology*, vol. 101, no. 1, pp. 276–282, 2009.
- [31] J. R. Vranish and E. F. Bailey, "A comprehensive assessment of genioglossus electromyographic activity in healthy adults," *Journal of Neurophysiology*, vol. 113, no. 7, pp. 2692–2699, 2015.
- [32] S. Hiyama, S. Iwamoto, T. Ono, Y. Ishiwata, and T. Kuroda, "Genioglossus muscle activity during rhythmic open–close jaw movements," *Journal of oral rehabilitation*, vol. 27, no. 8, pp. 664–670, 2000.
- [33] A. Malhotra, Y. Huang, R. B. Fogel, G. Pillar, J. K. Edwards, R. Kikinis, S. H. Loring, and D. P. White, "The male predisposition to pharyngeal collapse: importance of airway length," *American journal of respiratory and critical care medicine*, vol. 166, no. 10, pp. 1388–1395, 2002.
- [34] T. Corbett, B. Doyle, A. Callanan, M. Walsh, and T. McGloughlin, "Engineering silicone rubbers for in vitro studies: creating aaa models and ilt analogues with physiological properties," *Journal of biomechanical engineering*, vol. 132, no. 1, p. 011008, 2010.
- [35] T. Corcoran and N. Chigier, "Inertial deposition effects: a study of aerosol mechanics in the trachea using laser doppler velocimetry and fluorescent dye," *Journal of biomechanical engineering*, vol. 124, no. 6, pp. 629–637, 2002.
- [36] L. Hopkins, J. Kelly, A. Wexler, and A. Prasad, "Particle image velocimetry measurements in complex geometries," *Experiments in Fluids*, vol. 29, no. 1, pp. 91–95, 2000.

Appendices

Appendix A

Arduino Electronics Control Code

```
1 #include <Adafruit_Sensor.h>
2 #include <Adafruit_MMA8451.h>
3 #include <Servo.h>
4
5 // Mathematical Constants
6 double pi = 3.141592653589793238462643383;
7 // Pins
8 const int MS1 = 9;
9 const int MS2 = 10;
10 const int MS3 = 11;
11 const int STEP = 13;
12 const int DIR = 12;
13 const int ACT1 = 6;
14 const int ACT2 = 5;
15 const int ACT3 = 3;
16 // Stepper Driver A4988
17 const int stepSizeArrSize = 5;
18 const String stepSizeArr[stepSizeArrSize] = {"halfstep", "
    quarterstep", "eighthstep", "sixteenthstep", "fullstep"};
19 const String myStepSize = stepSizeArr[0];
20 const int forward = 1; // HIGH
21 const int backward = 0; // LOW
22 const float minPulseWidth = 1; // us
23 const float setupTime = 0.2; // us
24 const float holdTime = 0.2; // us
25 float stepTime = 20000; // us
26 // Hardware variables
27 float lead = 20; // mm, units should match supplied velocity
    length units
28 int stepsPerRev = 200; // Full step, will be changed in setup
    based on myStepSize
29 // Timing variables
```

```

30 float myClock = -1;
31 float now;
32 float stepperTimer;
33 float actuatorTimer;
34 boolean pause = false;
35 float cycleTime = 3000000 * 2; // us
36 float startTime = -1;
37 // Velocity time relationship variables
38 float maxVelocity = 2; // mm/s
39 float velocity = maxVelocity * sin((2 * pi) / (cycleTime) * (
    micros()))); // mm/s
40 // Useable variables for various things
41 float temp;
42 int count = 0;
43 String command;
44 int nPulses = 0;
45 float t;
46 // Actuator
47 float const ACTMINPULSE = 1050; // us
48 float const ACTMAXPULSE = 2000; // us
49 Servo act1, act2, act3;
50 // Accelerometer
51 Adafruit_MMA8451 mma = Adafruit_MMA8451();
52 float mmaXo = 0;
53 float mmaYo = 0;
54 float mmaZo = 0;
55 float aTheoretical; // Theoretical acceleration
56 float aActual; // Actual acceleration
57 float g;
58 // Sine wave
59 const float A = 10; // Max velocity mm/s
60 const float B = pi / 2; // Coefficient of t
61 const float T = 2 * pi / B; // Peroid of oscillation
62 const float F = 1 / T; // Frequency of oscillation
63 const float C = 0; // x axis offset
64 const float D = 0; // y axis offset
65 boolean oscillate = true;
66
67 void setup() {
68     // put your setup code here, to run once:
69     Serial.begin(2000000);
70     // Actuator
71     act1.attach(ACT1, ACTMINPULSE, ACTMAXPULSE);
72     act2.attach(ACT1, ACTMINPULSE, ACTMAXPULSE);
73     act3.attach(ACT1, ACTMINPULSE, ACTMAXPULSE);
74     act1.write(ACTMAXPULSE);
75     act2.write(ACTMAXPULSE);
76     act3.write(ACTMAXPULSE);

```

```

77 // Accelerometer
78 Serial.println("
    -----")
    ;
79 Serial.println("\t\tInitialise accelerometer");
80 if (! mma.begin()) {
81     Serial.println("Couldnt start");
82     //while (1);
83 }
84 else
85     Serial.println("MMA8451 found!");
86 mma.setRange(MMA8451_RANGE_8_G);
87 Serial.print("Range = "); Serial.print(2 << mma.getRange());
88 Serial.println("G");
89 // Set initial acceleration values to eliminate acceleration
    due to the Earth
90 mma.read();
91 sensors_event_t event;
92 mma.getEvent(&event);
93 mmaXo = event.acceleration.x;
94 mmaYo = event.acceleration.y;
95 mmaZo = event.acceleration.z;
96 Serial.println("Inital acceleration values due to gravity.");
97 Serial.print("X: \t"); Serial.print(mmaXo); Serial.print("\t");
98 Serial.print("Y: \t"); Serial.print(mmaYo); Serial.print("\t");
99 Serial.print("Z: \t"); Serial.print(mmaZo); Serial.print("\t");
100 Serial.println("m/s^2 ");
101 g = sqrt(pow(event.acceleration.x, 2) + pow(event.acceleration.
    y, 2) + pow(event.acceleration.z, 2));
102 Serial.print("Gravity: \t"); Serial.print(g); Serial.print("\t"
    );
103 Serial.println("m/s^2");
104 // Stepper
105 Serial.println("
    -----")
    ;
106 Serial.println("\t\tInitialise stepper");
107 pinMode(MS1, OUTPUT);
108 pinMode(MS2, OUTPUT);
109 pinMode(MS3, OUTPUT);
110 pinMode(STEP, OUTPUT);
111 pinMode(DIR, OUTPUT);
112 digitalWrite(DIR, forward);
113 setStepSize(myStepSize);
114 stepTime = 20000; // ns
115 // Commands
116 Serial.println("
    -----")

```

```

    ;
117  Serial.println("\t\tCommand List:");
118  Serial.println("<start>");
119  Serial.println("<stop>");
120  Serial.println("<setAccZero>");
121  Serial.println("<moveDistance(distance, speed, direction)>");
122  Serial.println("Note: All commands should be surrounded by
    arrow brackets as shown above.");
123  // End setup
124  Serial.println("
    -----")
    ;
125  delay(500);
126 }
127
128 void loop() {
129  // Command center
130  command = getCommand();
131  doCommand(command);
132  // Accelerometer
133  mma.read();
134  sensors_event_t event;
135  mma.getEvent(&event);
136  aActual = sqrt(pow(event.acceleration.x - mmaXo, 2) + pow(event
    .acceleration.y - mmaYo, 2) + pow(event.acceleration.z -
    mmaZo, 2));
137  //aActual = event.acceleration.x;
138  // Clock reset
139  if (myClock == -1) {
140    myClock = micros();
141    startTime = micros();
142  }
143  // Motor movement
144  now = micros();
145  temp = now - stepperTimer;
146  if (temp >= abs(stepTime) && pause == false) {
147    stepperTimer = now;
148    if (oscillate) {
149      myStep();
150      oscillateStepTime();
151    }
152    else if (nPulses != 0) {
153      myStep();
154      nPulses--;
155    }
156  }
157 }
158

```

```

159 void oscillateStepTime() {
160     t = micros() * pow(10, -6);
161     velocity = A * sin(B * t + C) + D; // mm/s
162     aTheoretical = A * B * cos(B * t + C);
163     if (velocity < 0.02 * A && velocity > -0.02 * A) {
164         return;
165     }
166     setStepTime(float(pow(10, 6)) * float(lead) / float(velocity *
        stepsPerRev)); // ns
167     if (stepTime < 0) {
168         setDirection(backward);
169     }
170     else {
171         setDirection(forward);
172     }
173     if (velocity < 0) {
174         aActual *= -1;
175     }
176     Serial.print(t, 6); Serial.print("\t"); Serial.print(velocity);
177     Serial.print(aTheoretical); Serial.print("\t"); Serial.println(
        aActual);
178 }
179
180 // -----
181 //                               Stepper motor functions
182 // -----
183 void myStep() {
184     digitalWrite(STEP, HIGH);
185     delayMicroseconds(minPulseWidth);
186     digitalWrite(STEP, LOW);
187     delayMicroseconds(minPulseWidth);
188 }
189
190 void setDirection(int _direction) {
191     if (_direction != 0 || _direction != 1) {
192         digitalWrite(DIR, _direction);
193         delayMicroseconds(setupTime);
194     }
195     else
196         Serial.println("Direction should be 1 (HIGH) or 0 (LOW)");
197 }
198
199 void setStepTime(float _stepTime) {
200     stepTime = _stepTime;
201 }
202
203 void moveDistance(float _distance, float _speed, int _dir) {

```

```
204  if (nPulses == 0) {
205      digitalWrite(DIR, _dir);
206      setStepTime(lead / (_speed * stepsPerRev)*pow(10, 6));
207      nPulses = _distance / lead * stepsPerRev;
208  }
209  else {
210      Serial.println("Still moving, wait your turn.");
211  }
212 }
213
214 void setStepSize(String str) {
215     if (pause == true) {
216         Serial.print("The curent step size is ");
217         str.toLowerCase();
218         str.replace(" ", "");
219         if (str == stepSizeArr[0]) {
220             digitalWrite(MS1, HIGH);
221             digitalWrite(MS2, LOW);
222             digitalWrite(MS3, LOW);
223             Serial.println(stepSizeArr[0] + ".");
224             stepsPerRev = 400;
225             delayMicroseconds(setupTime);
226         }
227         else if (str == stepSizeArr[1]) {
228             digitalWrite(MS1, LOW);
229             digitalWrite(MS2, HIGH);
230             digitalWrite(MS3, LOW);
231             Serial.println(stepSizeArr[1] + ".");
232             stepsPerRev = 800;
233             delayMicroseconds(setupTime);
234         }
235         else if (str == stepSizeArr[2]) {
236             digitalWrite(MS1, HIGH);
237             digitalWrite(MS2, HIGH);
238             digitalWrite(MS3, LOW);
239             Serial.println(stepSizeArr[2] + ".");
240             stepsPerRev = 1600;
241             delayMicroseconds(setupTime);
242         }
243         else if (str == stepSizeArr[3]) {
244             digitalWrite(MS1, HIGH);
245             digitalWrite(MS2, HIGH);
246             digitalWrite(MS3, HIGH);
247             Serial.println(stepSizeArr[3] + ".");
248             stepsPerRev = 3200;
249             delayMicroseconds(setupTime);
250         }
251         else if (str == stepSizeArr[4]) {
```

```

252     digitalWrite(MS1, LOW);
253     digitalWrite(MS2, LOW);
254     digitalWrite(MS3, LOW);
255     Serial.println(stepSizeArr[4] + ".");
256     stepsPerRev = 200;
257     delayMicroseconds(setupTime);
258 }
259 }
260 else {
261     Serial.println("Use the <stop> command before changing the
        step size.");
262 }
263 }
264
265 // -----
266 //                               GUI command center
267 // -----
268 void doCommand(String _command) {
269     if (_command.substring(0, 12) == "moveDistance") {
270         Serial.println(_command);
271         moveDistance(
272             _command.substring(_command.indexOf('(') + 1, _command.
                indexOf(',') + 1).toFloat(),
273             _command.substring(_command.indexOf(',') + 1, _command.
                indexOf(',', _command.indexOf(',') + 1)).toFloat(),
274             _command.substring(_command.lastIndexOf(',') + 1, _command.
                lastIndexof(')')).toFloat());
275     }
276     if (_command == "stop") {
277         pause = true;
278         Serial.println("Motor sequence terminated.");
279     }
280     if (_command == "start") {
281         myClock = -1;
282         pause = false;
283         Serial.println("Initialising motor startup.");
284     }
285     if (_command == "oscillate") {
286         oscillate = !oscillate;
287         startTime = micros();
288         Serial.print("Oscillate = "); Serial.println(oscillate);
289     }
290 }
291
292 String getCommand() {
293     const byte numChars = 32;
294     int index = 0;
295     char charArr[numChars];

```



```
296 char readChar;
297 char startMarker = '<';
298 char endMarker = '>';
299 boolean startReading = false;
300 boolean complete = false;
301 int count = 0;
302 command = "";
303 while (Serial.available() > 0) {
304     count++;
305     readChar = Serial.read();
306     if (startReading == true) {
307         if (readChar != endMarker) {
308             charArr[index] = readChar;
309             index++;
310             // Serial.print(readChar);
311             if (index > numChars) {
312                 Serial.println("Command too long");
313                 return "";
314             }
315         }
316         else {
317             charArr[index] = '\0'; // Terminate the string
318             // Serial.println(readChar);
319             command = charArr;
320             // Serial.println(charArr);
321             // Serial.println(myString);
322             for (int i = 0; i < stepSizeArrSize; i++) {
323                 if (command == stepSizeArr[i]) {
324                     setStepSize(command);
325                 }
326             }
327             return charArr;
328         }
329     }
330     else {
331         if (readChar == startMarker) {
332             startReading = true;
333         }
334     }
335     delay(1);
336 }
337 return "";
338 }
```